Improvement of Aerodynamic Characteristics of an Airfoil by Static Extended Trailing Edge

by

Md. Shariful Islam

A thesis submitted in partial fulfillment of the requirements for the degree of Master of Science in Mechanical Engineering

Khulna University of Engineering & Technology
Khulna 9203, Bangladesh

April 2017

Declaration

This is to certify that the thesis work entitled "Improvement of Aerodynamic Characteristics of an Airfoil by Static Extended Trailing Edge" has been carried out by Md. Shariful Islam in the Department of Mechanical Engineering, Khulna University of Engineering & Technology, Khulna, Bangladesh. The above thesis work on any part of this work has not been submitted anywhere for the award of any degree or diploma.

Signature of Supervisor

Signature of Candidate

Approval

This is to certify that the thesis work submitted by Md. Shariful Islam entitled "Improvement of Aerodynamic Characteristics of an Airfoil by Static Extended Trailing Edge" has been approved by the board of examiners for the partial fulfillment of the requirements for the degree of Master of Science in Mechanical Engineering in the Department of Mechanical Engineering, Khulna University of Engineering & Technology, Khulna, Bangladesh in April 2017.

BOARD OF EXAMINERS

1. Dr. Mohammad Mashud Professor Khulna University of Engineering & Technology	Chairman (Supervisor)
2. Md. Golam Kader Professor & Head of the Department Department of Mechanical Engineering Khulna University of Engineering & Technology	Member
3. Dr. Khandkar Aftab Hossain Professor Khulna University of Engineering & Technology	Member
4. Dr. Abdullah Al-Faruk Assistant Professor Khulna University of Engineering & Technology	Member
5. Dr. Md. Mizanur Rahman Assistant Professor University of Malaysia, Sabah	Member (External)

Acknowledgement

At first I want to express my gratefulness to the Almighty Allah who is the most kind hearted to all of his creatures. I would like to express my sincere gratitude to my supervisor Prof. Dr. Mohammad Mashud, Department of Mechanical Engineering, Khulna University of Engineering & Technology, for the continuous support to my project, for his patience, guidance, valuable suggestions and time. Thanks for encouraging and helping me to solve all the problems.

I would like to extend my thanks to the board of examiners and special thanks to Prof. Dr. Khandakar Aftab Hossain for his valuable time to give suggestion for finalizing the thesis report. Also I like to give thanks to the head of the department, Prof. Md. Golam Kader and Vice-Chancellor Prof. Dr. Muhammed Alamgir, for giving me the permission to use the laboratory facilities of this University and financial support. I would like to give thanks to Md. Asaduzzaman, Md. Fazle Rabbi and Md. Amzad Hossain faculty member of this department for their friendly co-operation throughout the work. My heartiest thanks to the staffs of Machine Shop, Welding Shop and Aerial Robotics & Aerodynamics Lab for their co-operation towards the completion of the work. Last but not least; I would like to thank my family for supporting me throughout my life.

Md. Shariful Islam
Roll No:1305551

Abstract

The objective of this work is to study the SETE as an alternative flow control technique for lift enhancement at a small drag penalty in cruise flight. The geometrical quantities, chord distribution and other properties are given in convenient analytical expressions.The experiment was about to enhance the lift of NACA0012 airfoil with static extended trailing edge (SETE). A thin sheet was introduced to the wing trailing edge as a mechanical device without changing the basic configuration of the wing. Calculations were done to compare the coefficient of lift using static extended trailing edge (SETE) with those of using flap. The effects of SETE on the wing aerodynamics are mainly due to modifications of the airfoil camber and the flow structure at the trailing edge. The lift enhancement by the SETE is, expectedly, due to the camber effect. It is speculated that the drag penalty of the SETE is small because it is usually embedded in the wake of the main airfoil. Experimental results are presented, including the lift and drag coefficient of the baseline NACA0012 airfoil model and of model with the SETE and Gurney flaps. The lift enhancement is achieved by the SETE, whereas the drag polar and lift-to-drag ration remains largely unchanged. The zero-lift drag and Oswald's efficiency are not significantly affected by the SETE. The benefit analysis for the SETE in cruise flight is given in comparison with Gurney flap.

Contents

LIST OF TABLES

LIST OF FIGURES

LIST OF ILLUSTRATIONS

Nomenclature

NACA	National Advisory Committee for Aeronautics
SETE	Static Extended Trailing Edge
CFD	Computational fluid dynamics
AOA	Angle of Attack
C_l	Coefficient of Lift
C_d	Coefficient of Drag
R_e	Reynolds Number
C_p	Coefficient of pressure

CHAPTER-1

Introduction

1.1 General Introduction

It has long been recognized that flaps can significantly alter wing aerodynamics for high lift generation. The primary concern of aerodynamics is to increase lift. Flaps and slats are the conventional lift enhancement device. But drag is also increase with increasing lift in conventional flaps. Introduction of small trailing edge devices have attracted considerable attention for lift enhancement. Small trailing edge devices like Gurney flaps, mini flaps or thin metallic sheet can be used for this purpose. Conventional flaps have larger drag; therefore they are mainly deployed for takeoff and landing and but not suitable in cruise flight. Small trailing edge devices like Gurney flaps and divergent trailing edges for lift enhancement have attracted considerable attention in aeronautical community. The Gurney flap was introduced by Liebeck[1] for aeronautical applications and considerable measurements and calculations have been performed to determine the aerodynamic characteristics of wings with Gurney flaps at low speeds[2]. Measurements were also made at high speeds[3]. Gurney-flap-type tabs have been used along with vortex generators to enhance lift and suppress flow separation for a single-slotted-flap airfoil at large flap deflection[4]. Microflaps that can change the deflection angle were used for flutter suppression[5]. To mimic the behavior of bird feathers during landing, a self-adjusting movable flap close to the trailing edge was proposed by Bechert et al. [6], which was able to maintain higher lift when stall occurs. A review on trailing edge devices and other control technologies is given by Stanewsky[7].

In this project static extended trailing edge will be used to increase lift. By using static extended trailing edge the main airfoil element remains unchanged, but it will extend at the trailing edge by attaching a thin splitting plate of suitable length. The extension can be an aluminum plate, composite sheet or any rigid material plate. As there is no change in airfoil element and no vibration is induced by introducing extended trailing edge, it is called static extended trailing edge.

1.2 Background

Simple hinged flaps were used in the 1930s, along with the arrival of the modern fast monoplane which had higher landing and takeoff speeds than the old biplanes. Travelling flaps also extend backwards, to increase the wing chord when deployed, increasing the wing area to help produce yet more lift. These began to appear just before World War II due to the efforts of many different individuals and organizations in the 1920s and 30s. The first slats were developed by Gustav Lachmann in 1918 and simultaneously by Handley-Page who received a patent in 1919. By the 1930s automatic slats had been developed, which opened or closed as needed according to the flight conditions. Typically they were operated by airflow pressure against the slat to close it, and small springs to open it at slower speeds when the dynamic pressure reduced, for example when the speed fell or the airflow reached a predetermined angle-of-attack on the wing.Extended trailing edge was used in a ceramic airfoil in 2007, by Tianshu Liu, J. Montefort, W. Liou, and S. R. Pantula; Western Michigan University, Kalamazoo, Michigan 49008. And Qamar A. Shams; NASA Langley Research Center, Hampton, Virginia 23681 [6].

1.3 High-Lift Devices

In aircraft design and aerospace engineering, a high-lift device is a component or mechanism on an aircraft's wing that increases the amount of lift produced by the wing. The device may be a fixed component, or a movable mechanism which is deployed when required. To achieve reasonable field performance while also obtaining efficient transonic cruise a fairly sophisticated high lift system is required [3]. Common movable high-lift devices include wing flaps and slats. Fixed devices include leading edge root extensions and boundary layer control systems, which are less commonly used.

1.3.1 Flaps

Flaps are a high lift device consisting of a hinged panel or panels mounted on the trailing edge of the wing. When extended, they increase the camber and, in most cases, the chord and surface area of the wing resulting in an increase of both lift and drag and a reduction of the stall speed. These factors result in an improvement in takeoff and landing performance. There are many different flap designs and configurations in use. Large aircraft sometimes incorporate more than one type, utilizing different flap designs on the inboard and outboard

sections of the wing. The following are descriptions of some of the more common flap designs:

- Plain Flap – The rear portion of the wing aerofoil rotates downwards on a simple hinge arrangement mounted at the front of the flap.
- Split Flap – The rear portion of the lower surface of the wing aerofoil hinges downwards from the leading edge of the flap, while the upper surface remains immobile.
- Slotted Flap – Similar to a Plain Flap but incorporates a gap between the flap and the wing to force high pressure air from below the wing over the upper surface of the flap. This helps reduce boundary layer separation and allows the airflow over the flap to remain laminar.
- Fowler Flap – A split flap that slides rearwards level for a distance prior to hinging downwards. It thereby first increases chord (and wing surface area) and then increases camber. This produces a flap which can optimize both takeoff (partial extension for optimal lift) and landing (full extension for optimal lift and drag) performance. This type of flap or one of its variations is found on most large aircraft.
- Double Slotted Fowler Flap – This design improves the performance of the Fowler flap by incorporating the boundary layer energizing features of the slotted flap.

1.3.2 Slats

Slats are extendable, high lift devices on the leading edge of the wings of some fixed wing aircraft. Their purpose is to increase lift during low speed operations such as takeoff, initial climb, approach and landing. They accomplish this by increasing both the surface area and the camber of the wing by deploying outwards and drooping downwards from the leading edge. In contrast, Krueger flaps increase wing camber by extending panels forward from the lower surface of the wing. Slats normally have several possible positions and extend progressively in concert with flap extension.

Slats are most often extended and retracted using hydraulically or electrically powered actuators. In some more simplistic designs, however, they are held in the retracted position by aerodynamic forces and use springs or counterweights for automatic extension at low speeds / high angles of attack.

1.4 Objectives

The goal of the study is to experimentally find out how to utilize passive flow separation techniques on an existing high lift device system being the airfoil flap system and also find out how to apply the separation control on high flap deflections where flow separation is eminent. The objective of this work is to study static extended trailing edge as an alternative flow control technique for lift enhancement at a small drag penalty in cruise flight. Also examine the comparison with Gurney flaps and conventional flaps. More specifically goal of this project is to investigate the performance improvements of the aerodynamic characteristics such as lift and drag of an airfoil.

1.5 Applications

The extended trailing edge is mostly an undesirable phenomenon and an effective extended trailing edge can be used for enhancing lift, dramatically reduce drag and can achieve very high C_l/C_d (infinity when $C_d = 0$) at low AOA (cruise), and very high lift and drag at high AOA(takeoff and landing); Significantly increase AOA operating range and stall margin; have small penalty to the propulsion system; can be applied to any airfoil, thick or thin; can be used for whole flying mission instead of only take-off and landing; can be used for low and high speed aircraft; easy implementation with no moving parts.

The above advantages of static extended trailing edge may derive the following superior aircraft performances:1) Extremely short distance for take-off and landing; 2) Supersonic aircraft to have small wing size matching cruise need, but also have high subsonic performance (e.g. high lift low drag at $M < 1$); 3) High maneuverability , high safety and fast acceleration military aircraft; 4) Very economic fuel consumption; 5) Small wing span for easy storage, light weight and reduced skin friction and form drag; 6) Low noise due to no high lift flap system and weakened wake mixing.

CHAPTER-2

Design & Construction

2.1 Methodology

Extended trailing edge is one of the most important research areas in the Aircraft mechanics that has been investigated by many researchers for more than 50 years. Measurements of avian wing geometry for extracting typical avian airfoil sections indicate that the merganser and owl wings have a very thin trailing edge that is a single layer of feathers extended from a 'normal' airfoil section [8]. Naturally, a question is whether and how this unique trailing edge affects the global aerodynamic characteristics of the wing. This inspires the concept of a static extended trailing edge as illustrated in Figure 2.1(a). The main airfoil element remains unchanged, but it is extended at the trailing edge by attaching a thin splitting plate of suitable length and rigidity. As shown in Figure 2.1(b), the basic geometrical parameters are the main airfoil chord (c), length of static extended trailing edge (l) and deflection angle (δ). Depending on specific applications, the extension could be an aluminum plate, polymer membrane, composite sheet or smart material plate. In general, a thin extended trailing edge is flexible such that it can be passively changed through flow-structure interaction or actively controlled by embedded actuators. In the current operating conditions, the analysis shows that when extended trailing edges are sufficiently rigid, their shapes are not sufficiently affected by flow and no vibration is induced. Thus, the cases studied here are static or quasi-steady. The effects of static extended trailing edge on the wing aerodynamics are mainly due to modifications of the airfoil camber and of the flow structure at the trailing edge. The lift enhancement by static extended trailing edge is expectedly due to the camber effect. It is speculated that the drag penalty of static extended trailing edge is small since it is usually embedded in the wake of the main airfoil. The drag penalty should be examined carefully in comparison with gurney flaps and conventional flaps. The objective of this work is to study the SETE as an alternative flow control technique for lift enhancement at a small drag penalty in cruise flight.

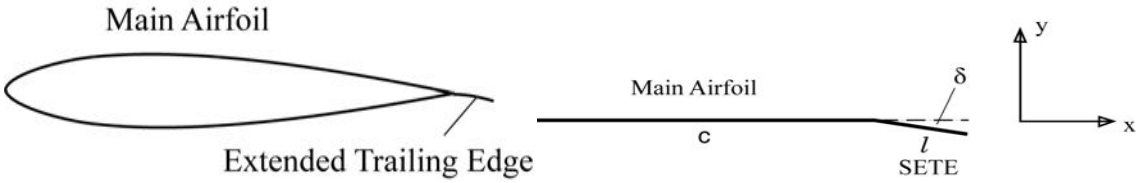

2(a) 2(b)

Figure 2.1 (a) Illustration of an extended trailing edge, (b) Geometrical parameters and coordinate system

2.2 Model Design:

Static extended trailing edge (SETE) airfoil geometry is slightly different from the conventional airfoil. The numbering system for SETE is defined first to construct the model. Here we carry our investigation on an airfoil which is modified from NACA0012. The airfoil nomenclature and design is given below.

(i) Airfoil Nomenclature:

The cross-sectional shape obtained by the intersection of the wing with the perpendicular plane is called an airfoil. The major design feature of an airfoil is the mean camber line, which is locus of points halfway between the upper and lower surfaces, as measured perpendicular to the mean camber line itself. The most forward points of the mean camber line are the leading and trailing edges, respectively. The straight line connecting the leading and trilling edges is the chord line of the airfoil, and the precise distance from the leading to the trilling edge measured along the chord line is simply designated the chord of the airfoil, given by the symbol c. The chamber is the maximum distance between the mean camber line and the chord line, measured perpendicular to the chord line. The camber, the shape of the mean camber line, and to a lesser extent, the thickness distribution of the airfoil essentially controls the lift and moment characteristics of the airfoil.

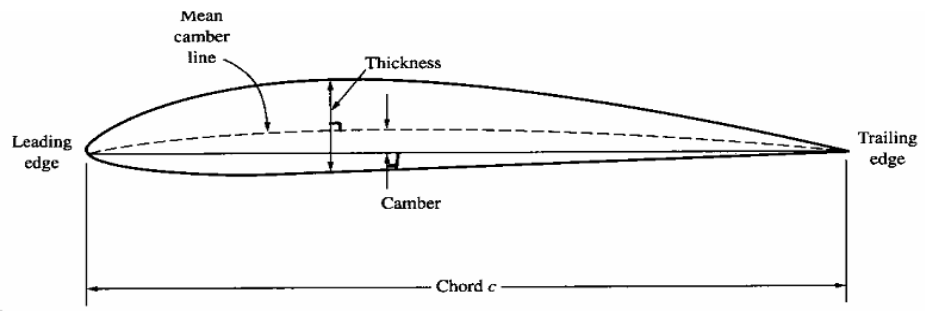

Figure 2.2 Airfoil nomenclature.

The numbering system for NACA 4-Digit airfoil is defined by:

NACA mpXX

Where,

XX is the maximum thickness, t/c, in percent chord.

m is the maximum value of the mean line in hundredths of chord,

p is the chord wise position of the maximum camber in tenths of the chord.

Note that although the numbering system implies integer values, the equations can provide 4 digit foils for arbitrary values of m, p, and XX.

(ii) SETE Airfoil Geometry:

A jet with a width of 2.5% the chord length is placed on a NACA0012 airfoil's upper surface simulating the blowing and suction control under $R_e=4.74x10^5$ and angle-of-attack 18^0condition. Nearly 300 numerical simulations are conducted over a range of parameters (Jet location, amplitude and angle). The physical mechanisms that govern suction and blowing flow control are determined and analyzed, and the critical values of suction and blowing locations, amplitudes, and angles are discussed. The current successful large-scale numerical studies create a useful knowledge base for further exploration of multi jet control system.

(iii) Airfoil Design:

Conventional NACA4 digit airfoil is designed by following steps:

1. Pick values of x from 0 to the maximum chord c.

2. Compute the mean camber line coordinates by plugging the values of m and p into the following equations for each of the x coordinates.

$$y_C=\frac{m}{p2}(2px-x^2) \qquad \text{From x=0 to x=p----------(2.1)}$$

$$y_C=\frac{m}{(1-p)2}[(1-2p)+2px-x^2] \qquad \text{From x=p to x=c----------(2.2)}$$

Where,

x = coordinates along the length of the airfoil, from 0 to c (which stands for chord, or length)

y = coordinates above and below the line extending along the length of the airfoil, these are either y_t for thickness coordinates or y_c for camber coordinates

m = maximum camber in tenths of the chord

p =position of the maximum camber along the chord in tenths of chord

3. Calculate the thickness distribution above (+) and below (-) the mean line by plugging the value of t into the following equation for each of the x coordinates.

$$\pm y_t=\frac{t}{0.2}(0.2969\sqrt{x}-0.1260x-0.3516x^2+0.2843x^3-0.1015x^4)\text{-------(2.3)}$$

4. Determine the final coordinates for the airfoil upper surface (x_u, y_u) and lower surface (x_l, y_l) using the following relationships.

$$x_U=x-y_t\sin\theta\text{----------(2.4)}$$

$$y_U=y_c+y_t\cos\theta\text{----------(2.5)}$$

$$x_L=x+y_t\sin\theta\text{----------(2.6)}$$

$$y_L=y_c-y_t\cos\theta\text{----------(2.7)}$$

$$\text{where, }\theta=\arctan(\frac{dy_c}{dx})\text{----------(2.8)}$$

2.3 Model Construction:

The NACA0012 well documented airfoil from the 4-digit series NACA airfoil, was utilized. The NACA 0012 airfoil is symmetrical; the 00 indicates that it was no camber.The 12 indicates that the airfoil has a 12% thickness to chord length ratio; it is 12% as thick as it is long. The pre-processor is a program that can be employed to produce models in two and three dimensions, using structured or unstructured meshes, which can consist of a variety of elements, such as quadrilateral, triangular or tetrahedral element. The resolution of the mesh was greater in regions where greater computational accuracy was needed, such as the region close to the airfoil.

The first step in performing a CFD simulation should be to investigate the effect of the mesh size on the solution results. Generally, a numerical solution becomes more accurate as more nodes are used, but using additional nodes also increases the required computer memory and computational time. The appropriate number of nodes can be determined by increasing the number of nodes until the mesh is sufficiently fine so that further refinement does not change the results.

This study revealed that a C-type grid topology with 80000 quadrilateral cells would be sufficient to establish a grid independent solution. The domain height was set to approximately 20 chord lengths and the height of the first cell adjacent to the surface was set to 10-5, corresponding to a maximum *y*+ of approximately 0.2. A *y*+ of this size should be sufficient to properly resolve the inner parts of the boundary layer. In order to include the transition effects in the aerodynamic coefficients calculation and get accurate results

for the drag coefficient, a new method was used. The transition point from laminar to turbulent flow on the airfoil was determined and the computational mesh was split in two regions, a laminar and a turbulent region. To calculate the transition point the following procedure was used. A random value for the transition point (X_{tr})was chosen and the computational domain was split at that point with a perpendicular line. The problem was simulated in Fluent after defining the left region as laminar and the right as turbulent zone. If the C_D simulation result was larger than the experimental data, it meant that the simulated turbulent zone was larger than the real and a new value for the transition point had to be chosen, righter than the initial one. Respectively, if the C_D simulation result was lower than the experimental data it meant that the simulated turbulent zone was smaller than the real and the transition point was more left. This procedure was repeated until two C_D simulated results came off, which should satisfy the inequality$C_{D,sim1}<C_{D,exp}<C_{D,sim2}$and $X_{tr1}<X_{tr}<X_{tr2}$. The linear interpolation of the mentioned values results the correct X_{tr}. The mesh was separated with the X_{tr} that was calculated in two regions as mentioned earlier and the simulated results were closer to the experimental data.

CHAPTER-3

Experimental Setup and Procedure

This chapter is dedicated to the description of the SETE airfoil and the modifications made to the existing systems to enable testing of the SETE airfoil. This section will also include the instrumentation and measurement techniques used in the wind tunnel experiments.

3.1 SETE Airfoil Description

The SETE airfoils used in testing at KUET were a modified NACA 0012. The NACA 0012 airfoil was chosen for its ease of manufacturing and relative thickness. The thickness made it easier to fit all instrumentation and duct work into the airfoil given the size constraints imposed by the one-meter by one-meter wind tunnel test section; however the SETE concept can be implemented on any airfoil geometry. The modified NACA 0012 airfoil used in testing had a span of 0.5m and a chord length of 0.3m. As shown in figure 3.1(b), the airfoil was modified by recessing the suction surface (upper surface).3.1(a) shows a cross section of NACA0012, 3.1(c) shows a NACA0012 airfoil with static extended trailing edge (SETE),3.1(d) shows a NACA0012 airfoil with flap. This recession opened up a slot towards the leading edge of the airfoil (injection slot) and another slot towards the trailing edge (suction slot). The slot towards the leading edge was used to inject air tangentially over the suction surface, while the slot towards the trailing edge was used to remove air tangentially from the suction surface. One modified airfoil SETE NACA 0012 and one Basic Airfoil NACA 0012 were tested. The injection slot and suction slot of Modified airfoil SETE NACA 0012 had the same slot height which is 0.195 m or 0.65% of chord length. The airfoils are named by their injection and suction slot sizes according to the convention SETE4digit-INJ-SUC. So the airfoil with the 1mm injection slot was named SETE0012-065-065.The reason the suction slot size was larger than the injection slot is because the density of the air being removed by the suction slot is less than the density of the air being injected. Therefore, to balance the mass flow rates, the suction

area has to be larger or the velocity greater. But the velocity is limited because the flow will eventually become choked.

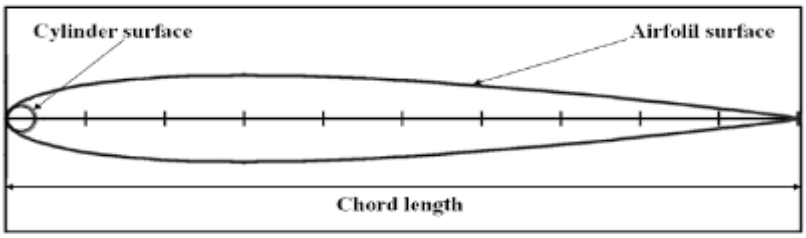

Figure 3.1 (a) Cross section of NACA0012

Figure 3.1(b)NACA0012 airfoil

Figure 3.1(c)NACA0012 airfoil with SETE

Figure 3.1(d)NACA0012 airfoil with Flap

The location of the injection slot and suction slot are respectively, 7.11% and 83.18% of the chord length from the leading edge. The slots are positioned perpendicular to the suction surface making them parallel to the flow direction.

3.2 Experimental Setup

The experiments are conducted using a 1m × 1m wind tunnel. Figure 3.2 illustrates the schematic diagram of the wind tunnel test section mounted with the cell model. The model is placed in the middle of the test section and supported with 4.0 mm diameter aluminum rod at the two circular holes of the side walls, so that it could freely rotate about the rod (if needed).

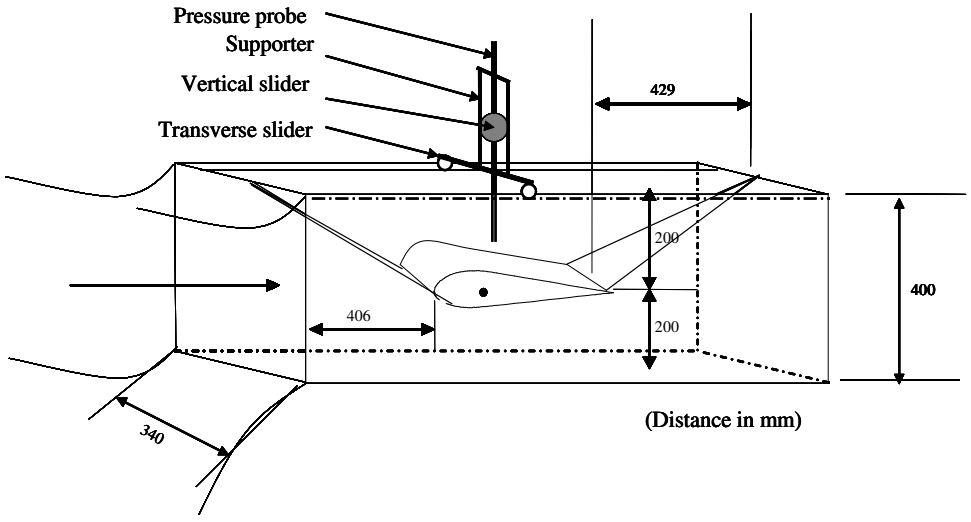

Figure 3.2: Wind tunnel test-section mounted with model

The orientation (change of attack angle) of the model is adjusted by pulling the two pairs of wires which suspend the leading and trailing edges of the rigid ribs. One sliding bar is also mounted over the test section for pressure measurement which will be discussed in the following section. Reynolds number *Re* is defined on the basis of the cord length *c* of the airfoil-shaped rib and the free stream velocity U_∞ of the test section. Reynolds number effects are examined by changing the free-stream velocity of the wind tunnel. The maximum Reynolds number is limited by the wind tunnel operating envelope, which is a maximum of about 14 m/s. The flow around the inflated cell model is visualized by the smoke wire method.

Figure 3.3: Modified Aerolab Wind Tunnel

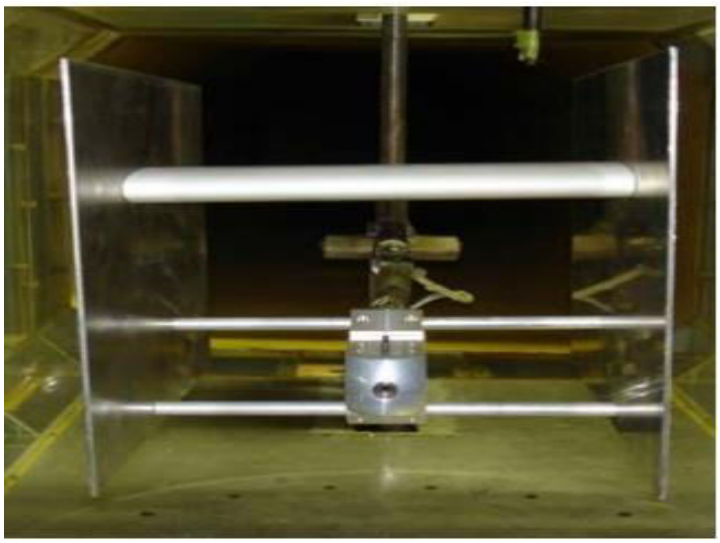

Figure 3.4: NACA0012 airfoil model mounted connected to a sting balance

Figure 3.5: Test Section of Modified Aerolab Wind Tunnel

Figure 3.6: Airfoil with extended trailing edge inside wind tunnel

Tests were conducted in the Modified Aerolab Wind Tunnel (MAWT) at Khulna University of Engineering & Technology (KUET). The MAWT is a low-speed, single-return atmospheric tunnel with a test section that is 1m high, 1m wide. Full-test-section length Plexiglas windows on the sides and ceiling allow optical access. The long circuit consists of two legs. Low turbulence and good flow direction control are obtained by a combination of features, including four screens and a honeycomb in the stilling chamber, a 10:1 contraction ratio between the stilling chamber and test section, empirically tailored test section walls, tangential flow breathing at the test section exit to the diffuser, and a 5.4 deg diffuser angle. Under the present test condition at $Re_c=4.74x10^5$, natural boundary

layer transition was observed at about 30% c on the NACA0012 airfoil model at a zero angle of attack (AOA) based on global luminescent-oil-film skin friction measurement. The main drive power source in a 30kw ac motor with a solid state speed controller. The 16 blade fan is 1m in diameter. The flow velocity range is approximately 0 to 80 m/s, in which the total temperature is in the range of 15 to 48^0C. This corresponds to the dynamic pressure up to 3.2 kN/m^2 and Reynolds numbers up to 4.74×10^5. Figure 3.3 shows the Modified Aero lab Wind Tunnel.

3.2.1 Pressure Measurement

The static pressure distribution on the surface of the wing cell model is measured by means of a digital pressure gauge, model GC 15-611 manufactured by Nagano Keiki Company Limited, and a pressure probe with an inner diameter of 0.5 mm and an outer diameter of 1.0 mm. The static and dynamic pressures measured at the inlet of test section are used as reference static and dynamic pressures, thus we could calculate the test section free-stream velocity. The reference static pressure is also used as reference for the pressure measuring system. The pressure is normalized by subtracting the reference pressure and divided by the free stream dynamic pressure $\frac{1}{2}\rho U_\infty^2$. The pressure coefficient $C_p$is defined by

$$C_p = \frac{P - P_\infty}{\frac{1}{2}\rho U_\infty^2} \quad \text{.....(3.1)}$$

Where,

P=Is the pressure measured at each point

P_∞= Is the reference static pressure

U_∞= Is the test section free-stream velocity

ρ = Is the air density during the experiment time

3.2.2 Mass Flow Rate Controls

The enhanced performance of the SETE airfoil comes from the air that is injected at the leading edge and removed at the trailing edge; therefore it is critical to control the injection and suction mass flow rates of air. The two mass flow rates were controlled in different manners due to the different systems available at the time of testing. A compressor supplied the air that was injected at the leading edge. The amount of air that passes through the injection slot is much less than the capability of the compressor .Therefore the

stagnation pressure is always constant. A wheel valve is used to control the air flow rate so that the injection mass flow rate is remaining constant which is measured and observed by a flow meter gauge. The suction mass flow rate was designed entirely different. The facilities at KUET did not include a vacuum pump designed to displace a large volume of air. Two vacuum pumps were available but they were designed to obtain a low pressure and hold it; to solve the problem, a high capacity vacuum pump was added onto the existing system. The addition of the new vacuum pump solved the vacuum pump deficiency; however the mass flow rate still needed to be controlled. The idea of choking the pipe prior to the vacuum tanks was chosen as the solution. A two-valve system was designed to accomplish this. The first valve was to open and close the pipe. This valve can be thought of as an on/off switch and was always in the fully open or fully closed position. The second valve, located closer to the vacuum tanks, was used to control the mass flow rate. This valve was a gate valve. A gate valve was chosen because of the greater accuracy in adjusting the effective flow area. Since the upstream stagnation pressure is constant, the inside area of the pipe is the only variable that effects the mass flow rate. The vacuum system must always be used in a choked condition to have a constant mass flow rate. The requirement for a choked system is the ratio of static pressure downstream of the valve to the stagnation pressure upstream of the valve to be less than 0.5283. So the system could only run until this requirement was no longer met. The injection and the suction mass flow rates were measured using orifice plates. Equation 3.1 relates the mass flow rate to the differential pressure across the orifice plate and the upstream density. Table 3.2 gives values for all constants in equation 3.2.

$$q_m=\frac{CE\varepsilon\pi d^2\sqrt{2\rho\Delta p}}{4} \quad \text{----------(3.2)}$$

where,

q_m= Mass flow rate

C= Discharge coefficient

$E=\frac{1}{\sqrt{1-\beta^4}}$=Velocity approach factor

β= Ratio of orifice diameter to inner pipe diameter

ε = Gas expansion factor

d= Orifice diameter

ρ_1= Upstream density

Δp= Differential pressure across orifice plate

Table 3.1: Orifice plate 1494 coefficients

Coefficient	Injection Side	Suction Side
C	0.6079	0.6117
E	1.048	1.111
Ɛ	0.9949	0.9659
D	1.682	2.026

The differential pressure was measured from the flanges housing the orifice plate. The upstream density was found by measuring the upstream temperature and pressure. Once the temperature, T , and pressure, P , were found, the density was obtained from the ideal gas law given in equation 3.3 with R being the gas constant for air.

$$\rho=\frac{P}{RT} \text{----------(3.3)}$$

A 0-1.27m H_2O differential pressure transducer was used to measure the differential pressure across the orifice plate. Only one 0-1.27m H_2O differential pressure transducer was available at the time of testing. Therefore it was impossible to measure two different mass flow rates simultaneously. A manual switch was implemented to go back and forth from measuring the injection and suction mass flow rates.

3.2.3 Balance Modifications

The balance used to measure lift and drag forces in the Aero lab wind tunnel was modified from a balance previously designed at the KUET. The main features of the balance will be described here. For an in-depth description of the balance and the calibration of the balance, the author refers the reader to reference 14.The balance was designed in such a way that when the angle of attack is changed, the airfoil does not cause a severe blockage in the wind tunnel. Although at extremely high angle of attacks, some blockage effects were unavoidable. The extent of the blockage was not taken into account. The free stream velocity was calculated from the dynamic pressure of the test section upstream the airfoil.

The balance was designed in such a way that the airfoil would not deflect more than 1mm on the free end. This was to ensure the strain on the cylinder supporting the airfoil was within the limits of the strain gauges (where lift and drag measurements are taken). In experiments, this 1mm deflection was exceeded. The deflection of the SETE airfoil is estimated to be 3mm; however exceeding this design parameter is not a concern.

The deflection is still small enough to allow for a small angle approximation for lift and drag. That is, lift is still assumed in the normal direction to the floor of the wind tunnel test section and drag is still assumed in the direction of the free stream. More importantly, the limitations of the strain gauges were not exceeded.

The balance was designed in such a way that the wires from the strain gauges could transverse through the side of the wind tunnel while the wind tunnel itself kept an airtight seal. The wind tunnel velocity is calculated from the dynamic pressure of the tunnel, so any air leaks into the tunnel could falsify the velocity reading. If there were airflow into the tunnel, the aerodynamic performance of the test airfoil would also be jeopardized. The basic design of the balance was kept. Compressed air was injected into the cylinder from a hose that was clamped on the free end outside the balance.

3.3 Calibration of Airfoil

The calibration of the airfoil was modified from a previous calibration procedure. The calibration procedure calibrates for lift, drag and pitching moment. However, it was later found the pitching moment was unreliable due to the latex tubes attached at the suction side of the airfoil. The calibration procedure is outlined here. An appropriate angle corresponds to an angle inside the airfoil's angle of attack margin. The SETE was tested from 0 deg to 30 deg, so an appropriate angle would fall anywhere between these two limits.

A metal calibration bar was then attached to the end of the clamps that holds the airfoil. The various aerodynamics properties were then measured with different AOA. The whole process was then repeated for different angle of attacks. The entire calibration process was then performed again to check for repeatability in the calibration curves. The variations in calibration curves are due to imperfection in the placement of the strain gauges on the metal cylinder and bonding of the strain gauges to the metal cylinder. Other imperfections include the solder joints and minute differences in the strain gauges themselves.

3.4 Uncertainty Analysis

This section is dedicated to the uncertainty analysis of all measured and calculated values. The uncertainties of the measured values are determined first. The uncertainties

of the calculated values are then found using the uncertainties of the measured values. The measured uncertainties were found using equations 3.4, 3.5 and 3.6. In the equations *U* represents the total uncertainty, *B* represents the bias uncertainty and *P* represents the precision uncertainty. The uncertainties of the measured values are summarized in table3.2.

$$U=\sqrt{B^2+(t_{V.95}P)^2} \text{----------(3.4)}$$

$$B=\sqrt{(B_1^2+B_2^2+\cdots+B_M^2)} \text{----------(3.5)}$$

$$P=\sqrt{(P_1^2+P_2^2+\cdots+P_N^2)} \text{----------(3.6)}$$

The calculated uncertainties were found using equation (3.7) and (3.8)

$$R=R(x_1,x_2,\ldots\ldots,x_f) \text{----------(3.7)}$$

$$U_R=\sqrt{(\frac{\partial R}{\partial X_1}U_{x_1})^2+(\frac{\partial R}{\partial X_2}U_{x_2})^2+\cdots+(\frac{\partial R}{\partial X_f}U_{x_f})^2} \text{----------(3.8)}$$

Table 3.2: List of Uncertainties of the measured values

Measurement	Uncertainty
Dynamic pressure from wind tunnel	0.35 mm H_2O
Differential pressure across orifice plate	3.4 mm H_2O
Static pressure in injection pipe	0.7 kpa
Static pressure in suction pipe	0.63 kpa
Stagnation pressure in injection slot	3.81 kpa
Static pressure in suction manifold	2 kpa
Static temperature in injection pipe	1.170^0 C
Static temperature in suction pipe	0.730^0 C
Static temperature in injection duct of airfoil	0.730^0 C
Static temperature in suction duct of airfoil	0.730^0 C
Lift force, C_l	0.0088-0.043
Drag force, C_d	0.0088-0.043

The wind tunnel velocity is found from the dynamic pressure. The velocity was calculated using equation (3.9)

$$V=\sqrt{\frac{2q}{\rho}}\text{----------(3.9)}$$

Where,V= Wind tunnel velocity

q= Dynamic pressure

ρ= Density of free stream

The uncertainty in the velocity measurement reduces to equations (3.10). the uncertainty in the velocity measurement is 0.748m/s or 2.08%. The velocity of the wind tunnel was also checked with PIV. The velocity measured from PIV was the uncertainty.

$$U_v=\sqrt{(\frac{\partial v}{\partial q}U_q)^2+(\frac{\partial v}{\partial \rho}U_\rho)^2}\text{----------(3.10)}$$

The mass flow rate was given by equation (3.2). The uncertainty of the mass flow rate can be reduced to equation (3.11). Table (3.3) shows values for the given uncertainties.

$$\frac{\partial q_m}{q_m}=((\frac{\partial C}{C})^2+(\frac{\partial \varepsilon}{\varepsilon})^2+(\frac{2\beta^4}{1-\beta^4})^2(\frac{\partial D}{D})^2+(\frac{2}{1-\beta^4})^2(\frac{\partial d}{d})^2+\frac{1}{4}(\frac{\partial \Delta p}{\Delta p})^2+\frac{1}{4}(\frac{\partial \rho_1}{\rho_1})^2)^{\frac{1}{2}}\text{---(3.11)}$$

Table 3.3: Uncertainty in orifice plate calculation

Coefficient	Uncertainty of Injection Side, %	Uncertainty of Suction Side, %
$\frac{\partial C}{C}$	0.06	0.06
$\frac{\partial \varepsilon}{\varepsilon}$	0.144	0.144
$\left(\frac{2\beta^4}{1-\beta^4}\right)^2\left(\frac{\partial D}{D}\right)^2$	≈0	≈0
$(\frac{2}{1-\beta^4})^2(\frac{\partial d}{d})^2$	≈0	≈0
$\frac{\partial \Delta p}{\Delta p}$	1.914	2.197
$\frac{\partial \rho_1}{\rho_1}=\sqrt{((\frac{\partial \rho_1}{\rho_1})^2+(\frac{\partial T_1}{T_1})^2)}$	0.562	0.870

The uncertainty in the mass flow rate measurement is 1.01% for the injection and 1.19% for the suction. The uncertainty in A/A^* needs to be found before the uncertainty of the

injection velocity can be determined. Equation (3.4) defined A/A*. The uncertainty of this ratio is given in equation (3.12)

$$U_{A/A^*}=\sqrt{((\frac{\partial(\frac{A}{A^*})}{\partial\rho_0}U\rho_o)^2+(\frac{\partial(\frac{A}{A^*})}{\partial q_m}Uq_m)^2+(\frac{\partial(\frac{A}{A^*})}{\partial T_0}U_{T_O})^2)}\text{----------(3.12)}$$

The jet momentum coefficient is the last quantity for which the uncertainty needs to be calculated. The jet momentum coefficient was defined in equation (3.13)

$$U_{C_\mu}=\sqrt{((\frac{\partial(C_\mu)}{\partial v_{jet}}Uv_{jet})^2+(\frac{\partial(C_\mu)}{\partial q_m}Uq_m)^2+(\frac{\partial(C_\mu)}{\partial v_\infty}U_{v_\infty})^2)}\text{----------(3.13)}$$

The uncertainty of the jet momentum coefficient is calculated to be 4.59%.The uncertainty of the lift and drag was calculated using Student's t-distribution [15], which is given in equation (3.14). Student's t-distribution gives the uncertainty of the true mean.

The uncertainty in A/A* is calculated to be 1.37%. This relates to an uncertainty in the Mach number of 1.65%. This uncertainty relates directly to the uncertainty of the velocity because the speed of sound, a, is considered constant. So the uncertainty of the injection velocity is 1.65%

$$\Delta=\frac{t\sigma}{\sqrt{n}}\text{----------(3.14)}$$

Where,

Δ= Uncertainty

t= t-value for corresponding confidence level

σ= Standard deviation

n= Number of samples

For a 95% confidence level and 50 samples, the t-value is equal to 2.0105. The standard deviation for both lift and drag at lower angle of attacks is 1 N and at higher angle of attacks is 5 N. This corresponds to standard deviation in terms of C_l and $C_d$of 0.031-0.153. So, the uncertainty in C_l and C_d would then be 0.0088 at lower angle of attacks and 0.043 at higher angle of attacks.

3.5 Procedure

This section describes the experimental procedure followed during the testing of the CFJ airfoils. The airfoils were tested in two configurations. The SETE0012-065-065 along with a baseline airfoil. The airfoils were also tested in two different manners. The airfoils were tested for lift and drag characteristics with strain gauges and flow field

visualization with smoke generation. Figure 3.7 Shows the curve for velocity calculation where x is applied voltage which is identical for testing lab.

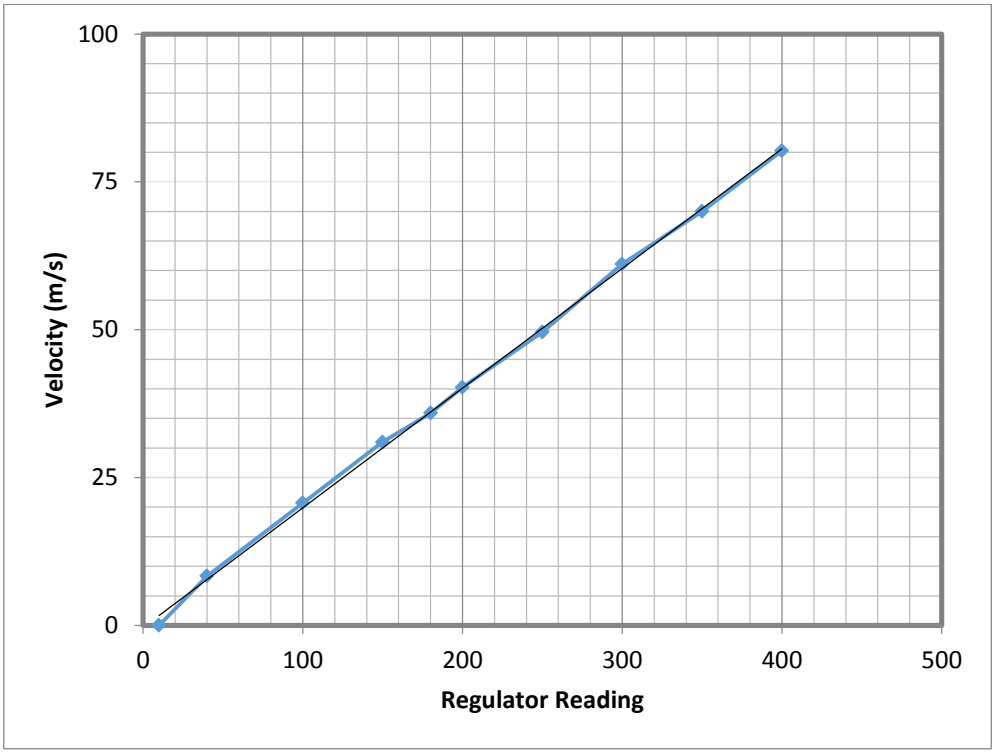

Figure-3.7: Curve for velocity calculation

The lift and drag testing is discussed first. A rigorous airfoil assembly procedure and testing procedure can be found. The airfoil to be tested would have to be assembled and placed into the wind tunnel. Once the airfoil was in the wind tunnel, the procedure was as follows:

i)At first NACA 0012 airfoil was constructed of designed chord and wingspan.

ii) Then the airfoil was prepared for the experiment and was placed in the wind tunnel.

iii) Pressure was measured for both upper & lower surfaces at different angle of attack (AOA) by using computer.

iv) Then coefficient of pressure was measured on both upper& lower surfaces for different angle of attack (AOA).

v) Coefficient of pressure curve with respect to distance along chord line was shown in the graph.

vi) Coefficient of lift was calculated from coefficient of pressure using necessary formula.

vii) The relation of coefficient of lift with respect to angle of attack was shown in graph.

viii) Then trailing edge was extended by attaching a thin Galvanized Iron sheet.

ix) The airfoil along with extended trailing edge was prepared for the experiment and was placed in the wind tunnel.

x) Procedure iii), iv), v), vi) & vii) was repeated for extended trailing edge.

xi) Then the designed flap was attached to the airfoil.

xii) The airfoil along with flap was prepared for the experiment and was placed in the wind tunnel.

xiii) Procedure iii), iv), v), vi) & vii) was repeated for airfoil with flap.

xiv) Finally the lift for NACA0012 airfoil, airfoil with extended trailing edge and airfoil with flap was compared and the comparison was shown by graph.

xv) Repeat the same procedure to justify the fluctuation of uncertainty and identify the correct data.

CHAPTER-4

Experimental Results

In this section we describe the measuring methods which are used to find out the aerodynamic characteristics and shape analysis of the paraglide canopy cell model. We are conducted different experiment in different condition and the experimental results are presented below a graphical form.

4.1 External Surface Pressure Distribution

The external surface pressure distribution is measured for various attack angles. Figure 4.9 shows the upper surface pressure coefficient $C_{pe,U}$ and lower surface pressure coefficient $C_{pe,L}$ at different attack angles. It has a property similar with the surface pressure distribution for a rigid wing at various attack angles.

The wind tunnel velocity was calculated from the dynamic pressure, $0.5\rho v^2$ of the test section. A 0-15 in H_2O differential pressure transducer was used to measure the dynamic pressure by measuring the difference between the static pressure in the test section upstream of the airfoil and the stagnation pressure in the room. The velocity was multiplied by a correction factor, found from previous experiments, to account for the losses in stagnation pressure that occur in the tunnel inlet.

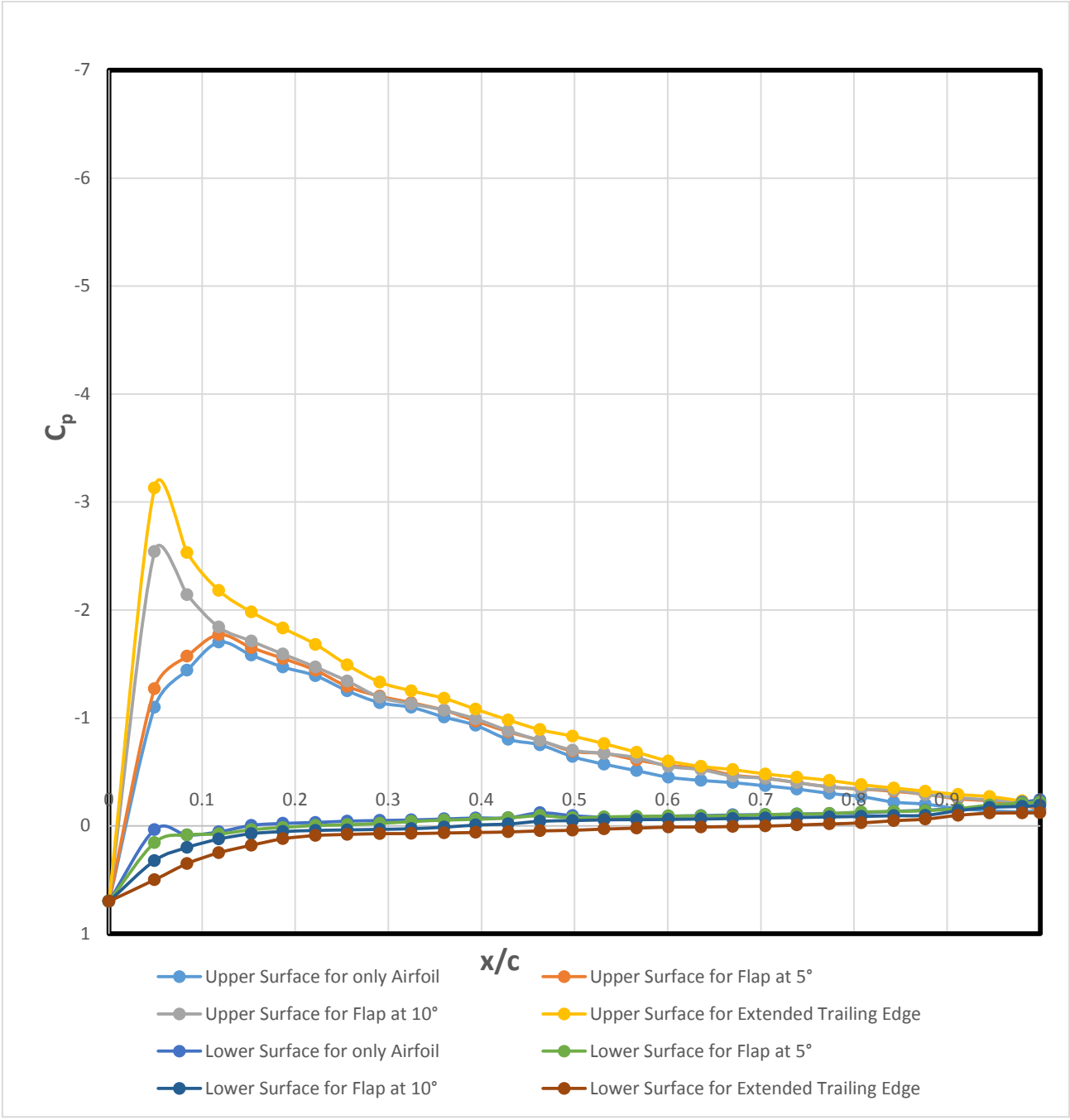

Figure-4.1: Coefficient of pressure vs distance for 0 degree AOA

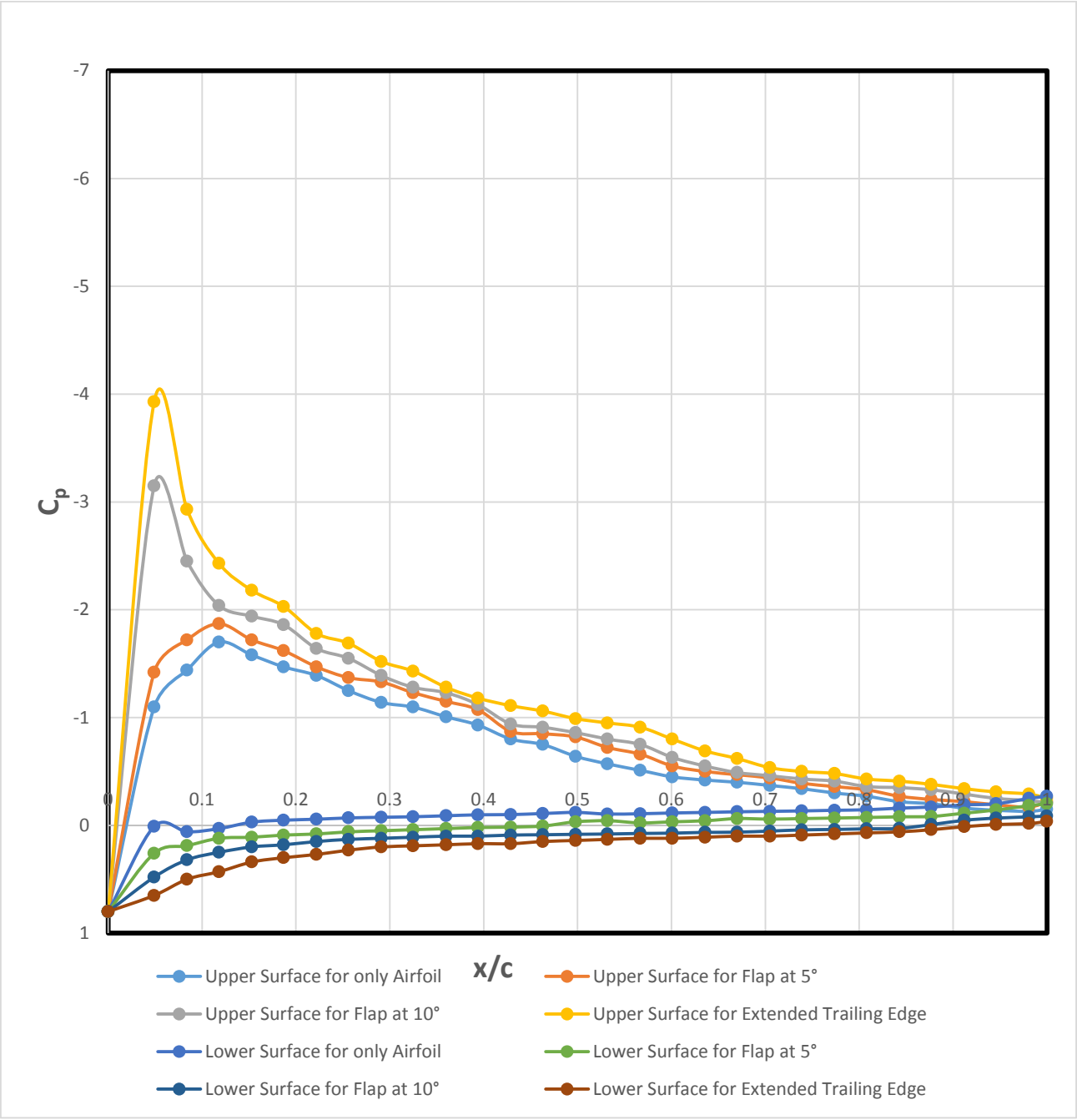

Figure-4.2: Coefficient of pressure vs distance for 2 degree AOA

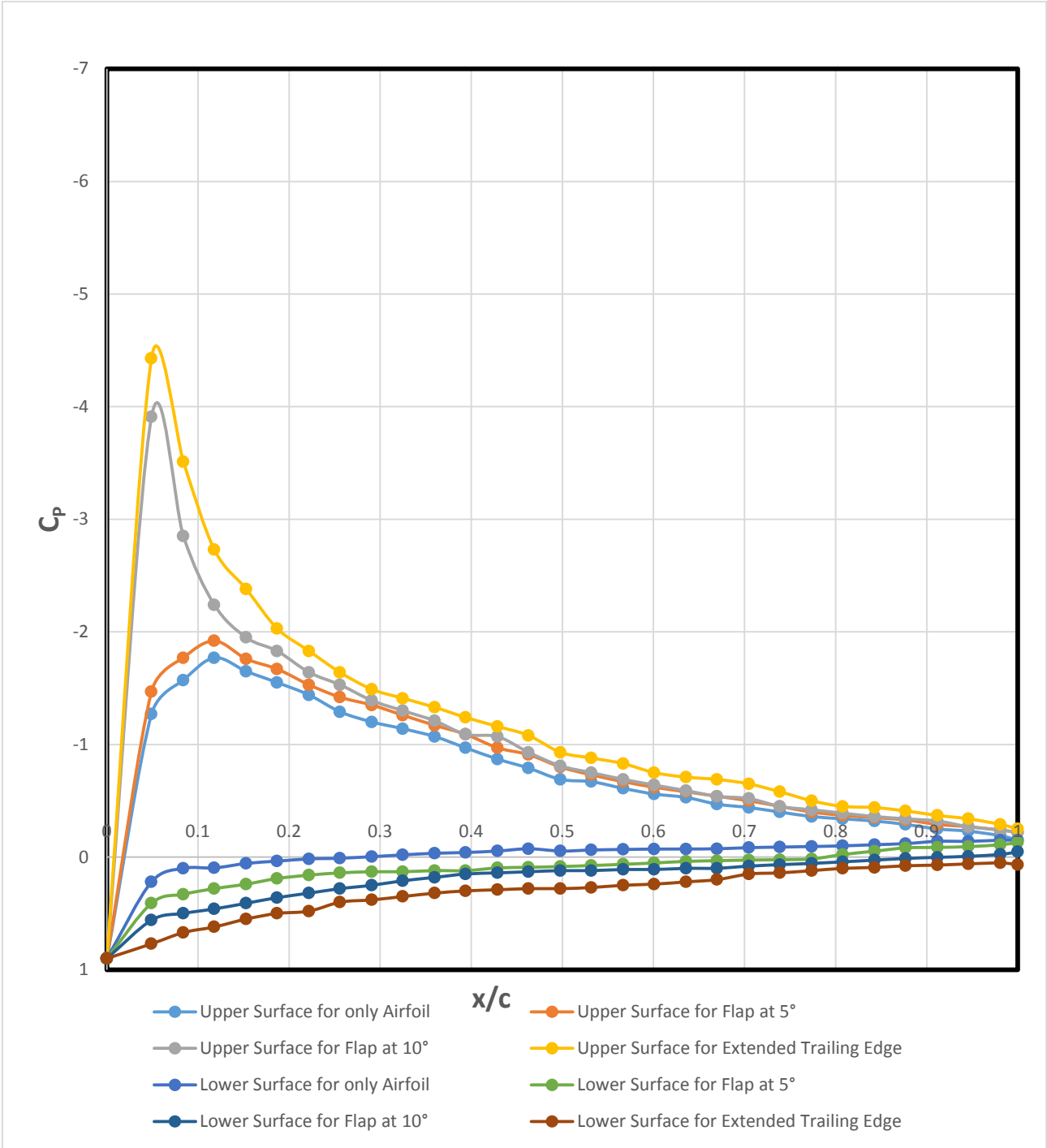

Figure-4.3: Coefficient of pressure vs distance for 4 degree AOA

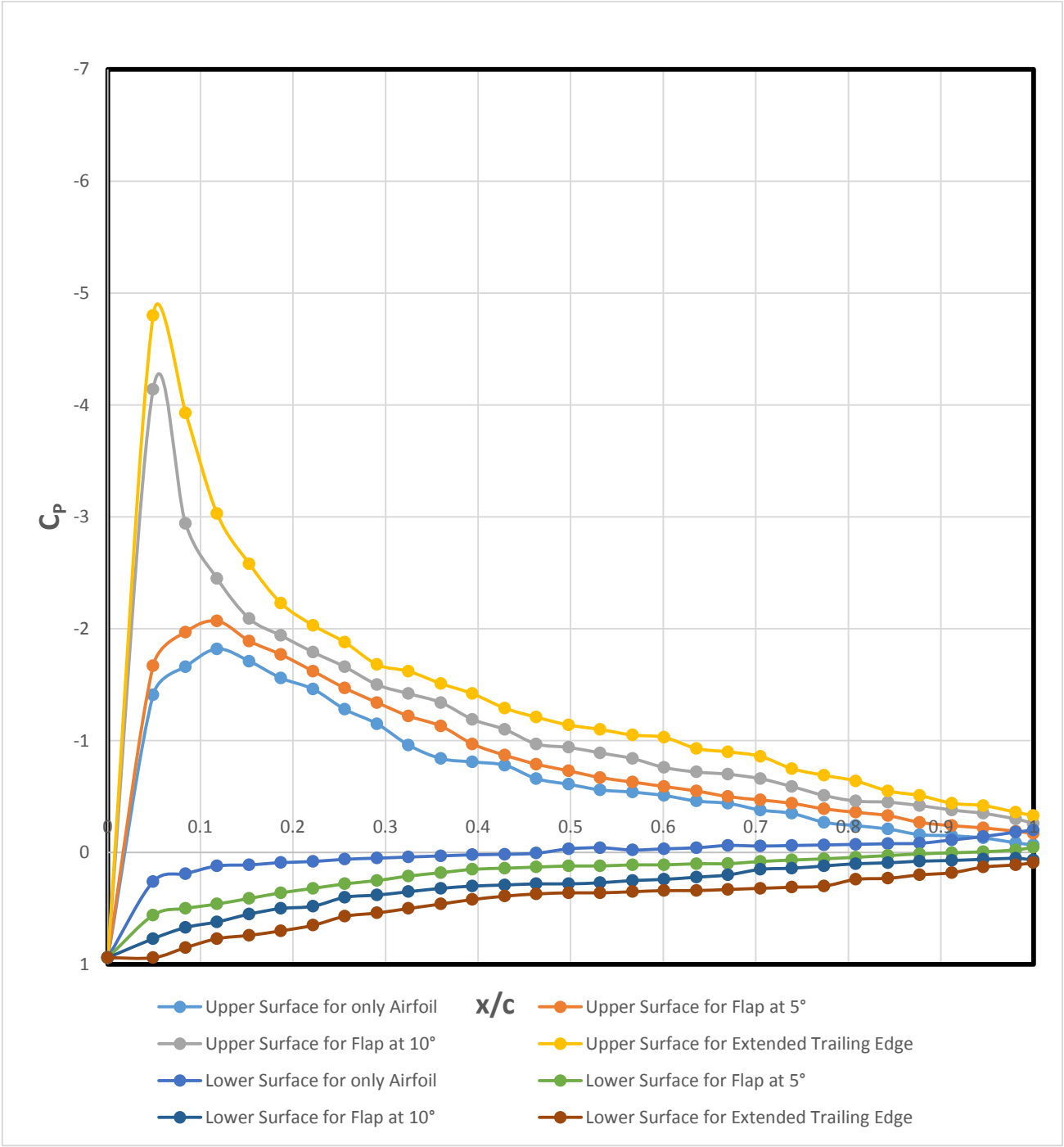

Figure-4.4: Coefficient of pressure vs distance for 6 degree AOA

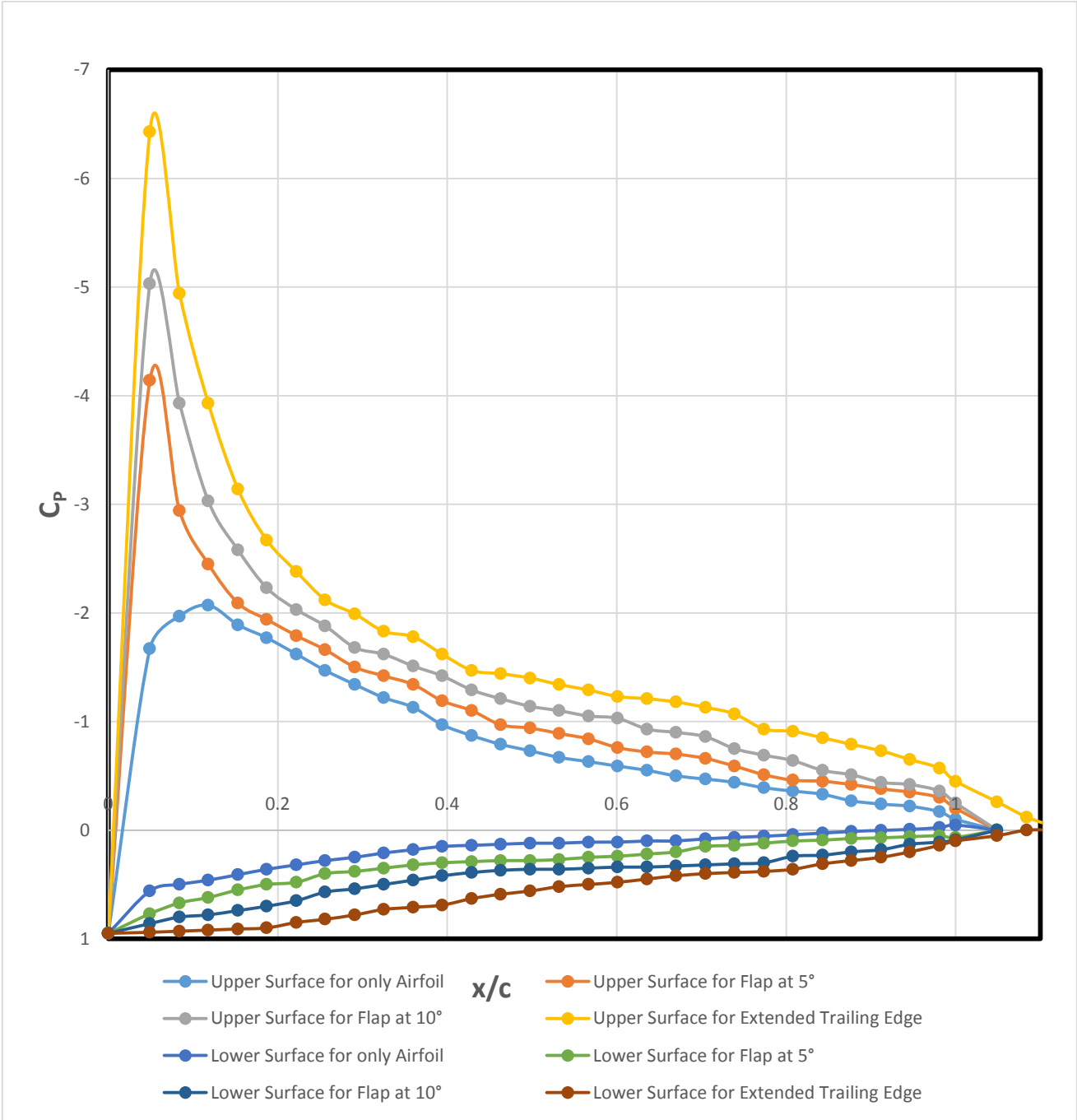

Figure-4.5: Coefficient of pressure vs distance for 8 degree AOA

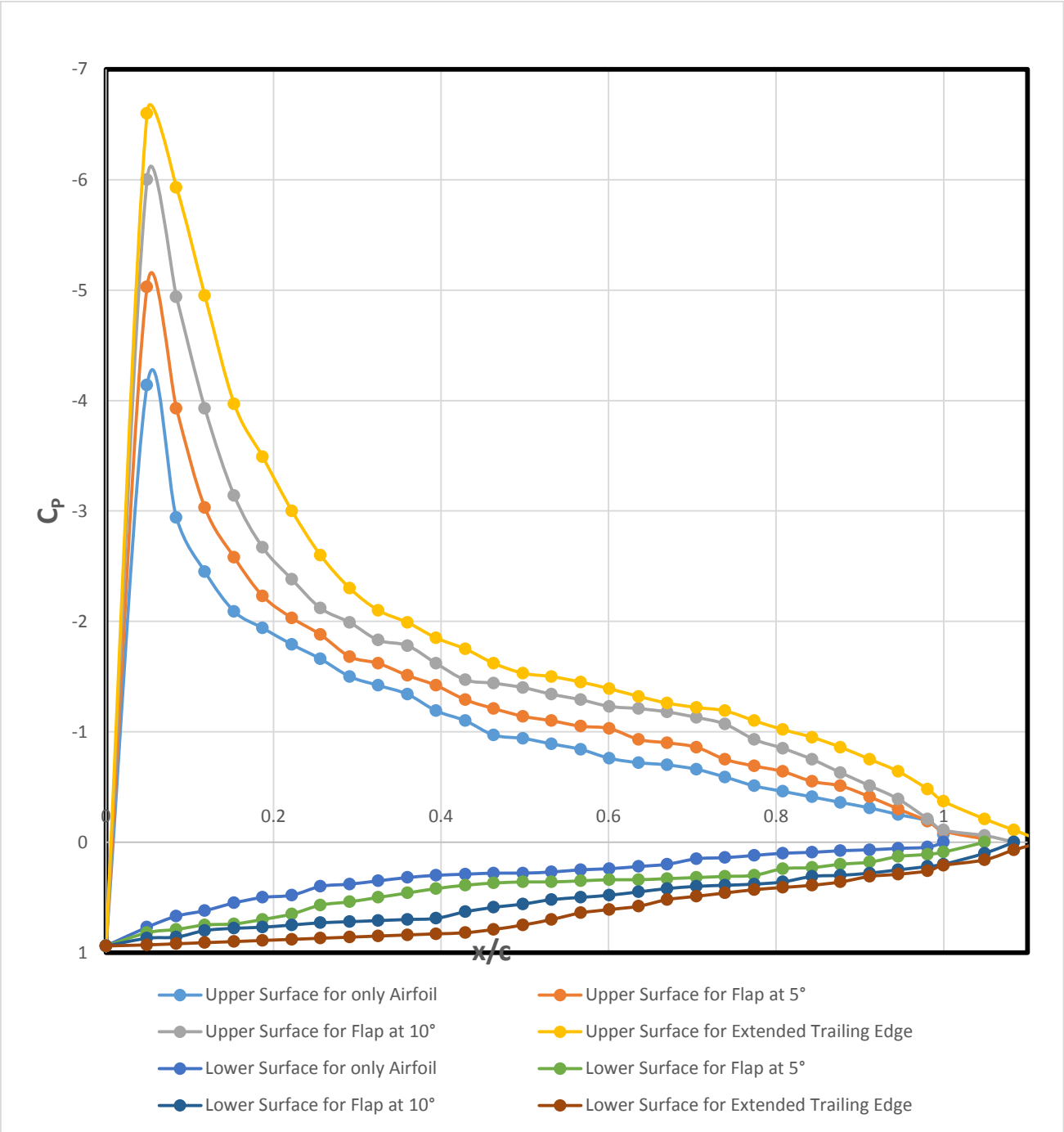

Figure-4.6: Coefficient of pressure vs distance for 10 degree AOA

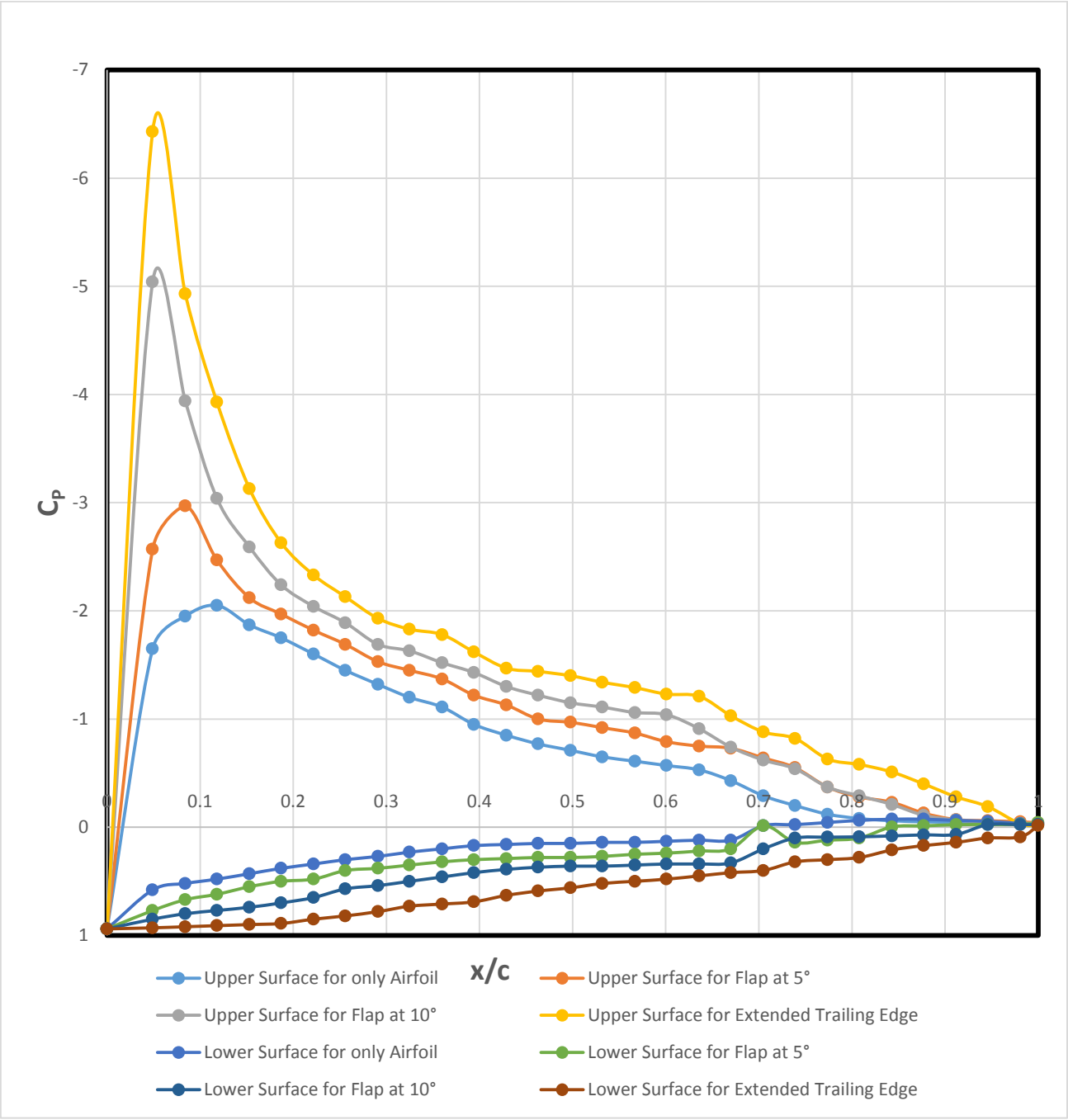

Figure-4.7: Coefficient of pressure vs distance for 12 degree AOA

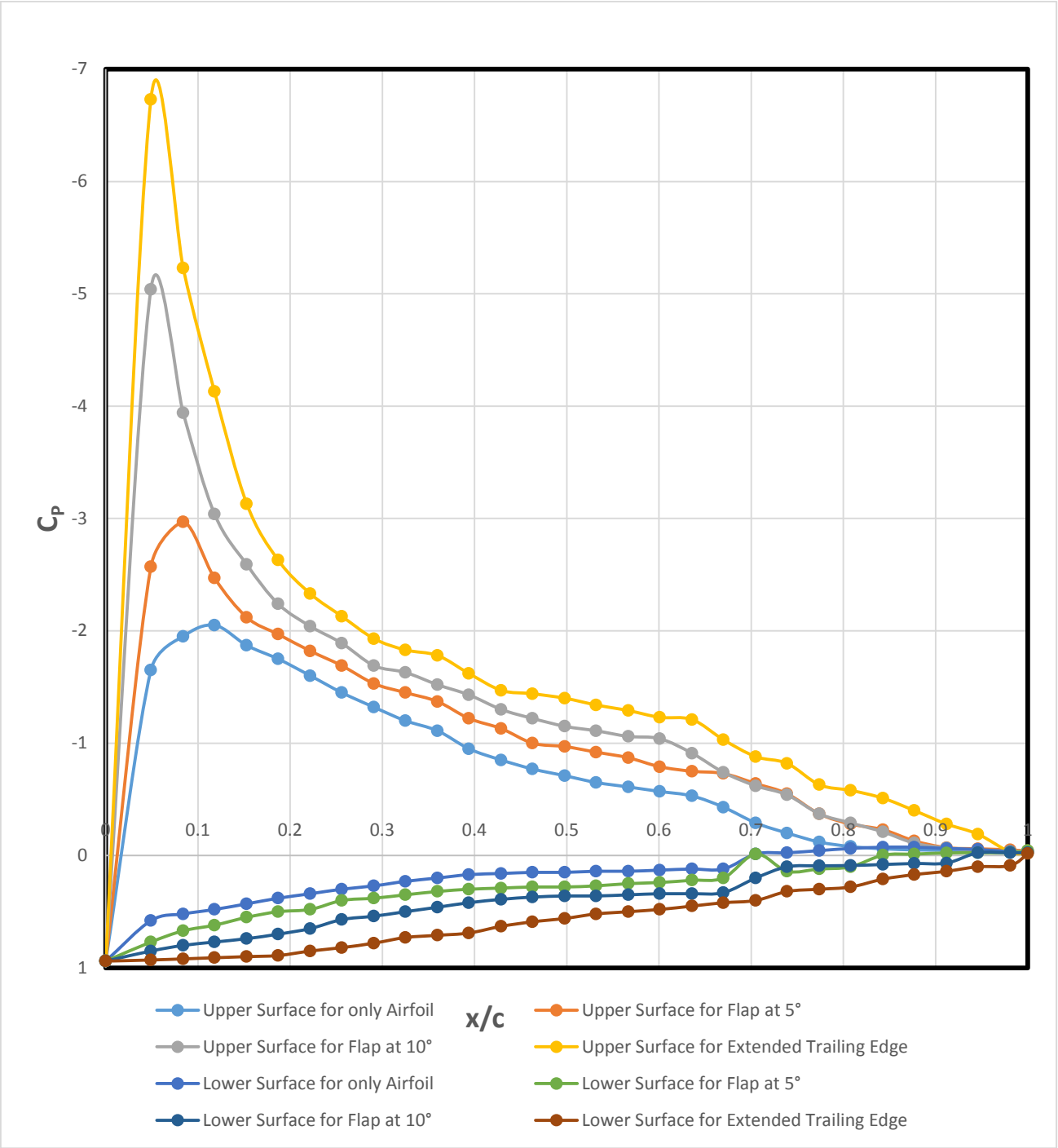

Figure-4.8: Coefficient of pressure vs distance for 14 degree AOA

4.2 Lift and Drag Coefficient

The aerodynamic forces on the body are due entirely to the two basic sources, firstly pressure distribution over the body surface, and secondly shear stress distribution over the body surface. The net effect of the pressure and shear stress distributions integrated over the complete body surface is a resultant aerodynamic force. In the present study, the lift and drag coefficients are calculated only on the basis of the measured internal and external pressure distributions on the body surfaces. Using the surface pressure distributions and the inflated canopy cell profile shown in Figure4.13, the lift coefficient c_l and drag coefficient c_d for the inflated canopy cell profile at the mid-span/central section can be calculated according to

$$C_l = \int_{-x_U}^{0} \left(C_{pi,U} - C_{pe,U}\right) dx + \int_{-x_L}^{0} \left(C_{pe,L} - C_{pi,L}\right) dx$$

$$\approx \int_{-x_U}^{-x_L} \left(C_{pi,U} - C_{pe,U}\right) dx + \int_{-x_L}^{0} \left(C_{pe,L} - C_{pi,L}\right) dx$$

$$\approx \int_{-x_U}^{0} C_{pe,U} dx + \int_{-x_L}^{0} C_{pe,L} dx + \overline{C_{pl}}(x_U - x_L) \text{----------(4.1)}$$

$$C_d = \int_{-x_U}^{0} \left(C_{pe,U} - C_{pi,U}\right) \frac{dy_U}{dx} dx + \int_{-x_L}^{0} \left(C_{pi,L} - C_{pe,L}\right) \frac{dy_L}{dx} dx$$

$$\approx \int_{-x_U}^{0} C_{pe,U} \frac{dy_U}{dx} dx - \int_{-x_L}^{0} C_{pe,L} \frac{dy_L}{dx} dx + \overline{C_{pl}}[y_U(x = -x_U) - y_L(x = -x_L)] \text{-------(4.2)}$$

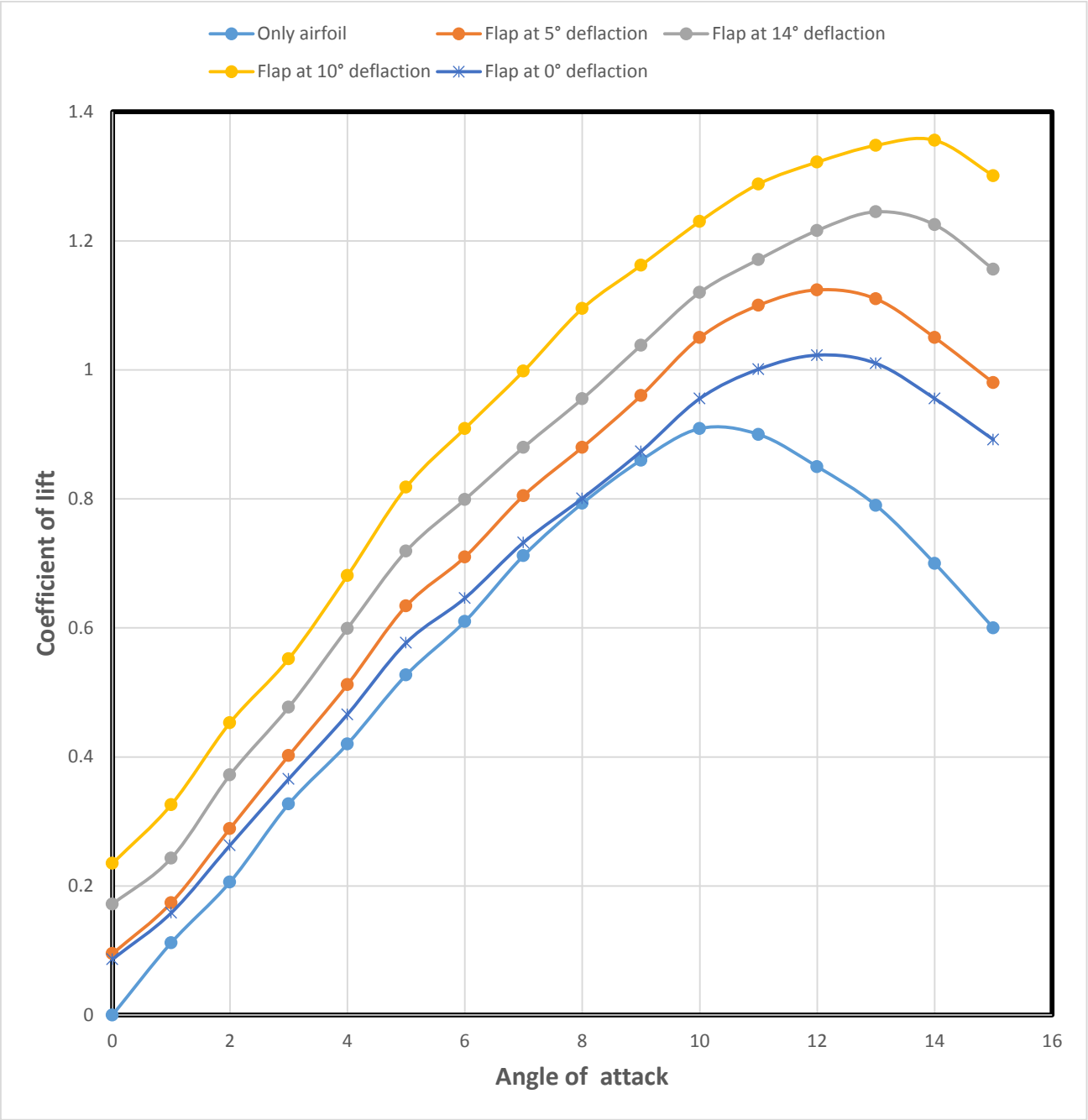

Figure-4.9: Comparison of coefficient of lift for only airfoil, airfoil attached with flap at different angle

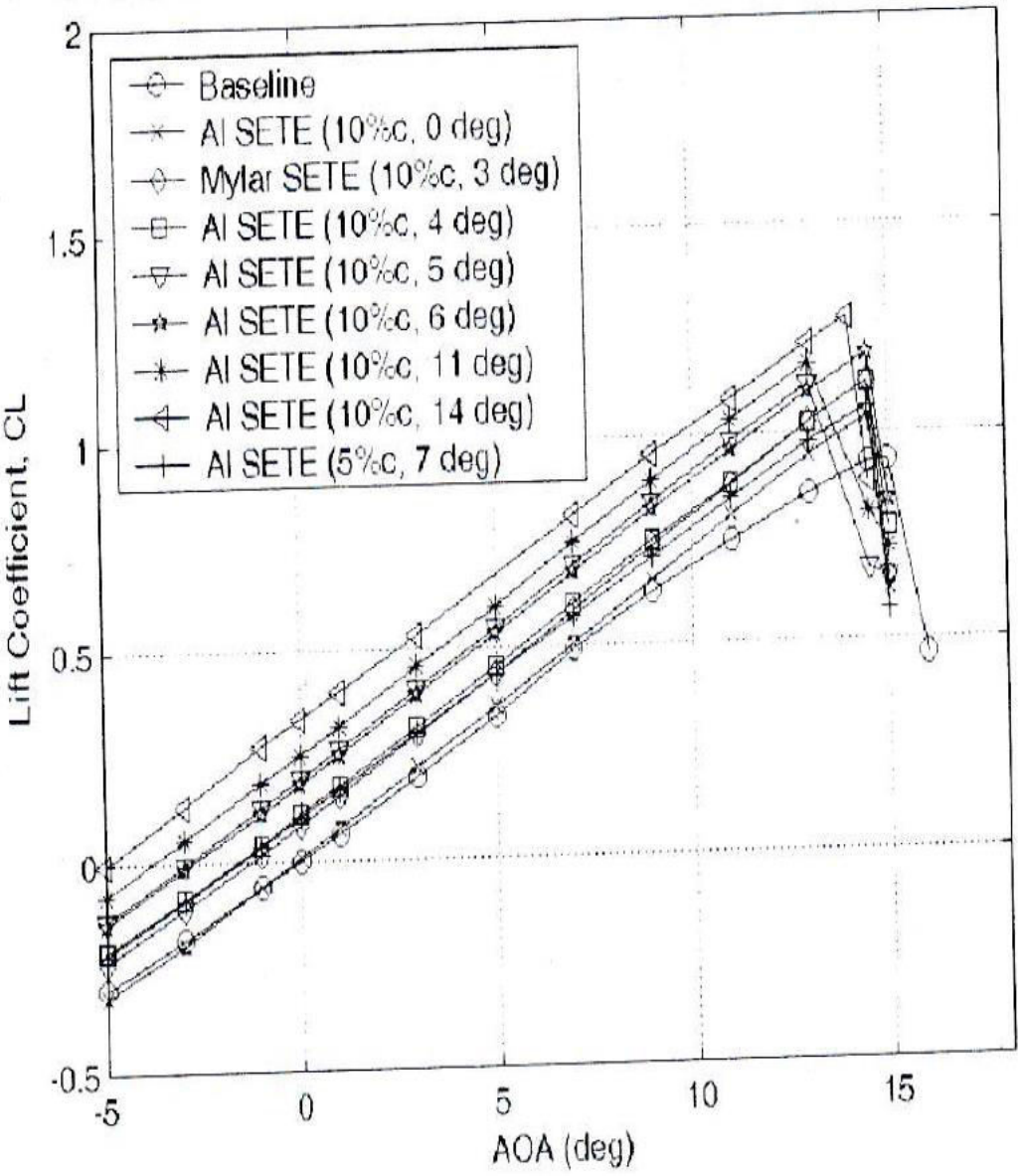

Figure-4.10: Lift Coefficient to AOA Collected from Journal of Aircraft

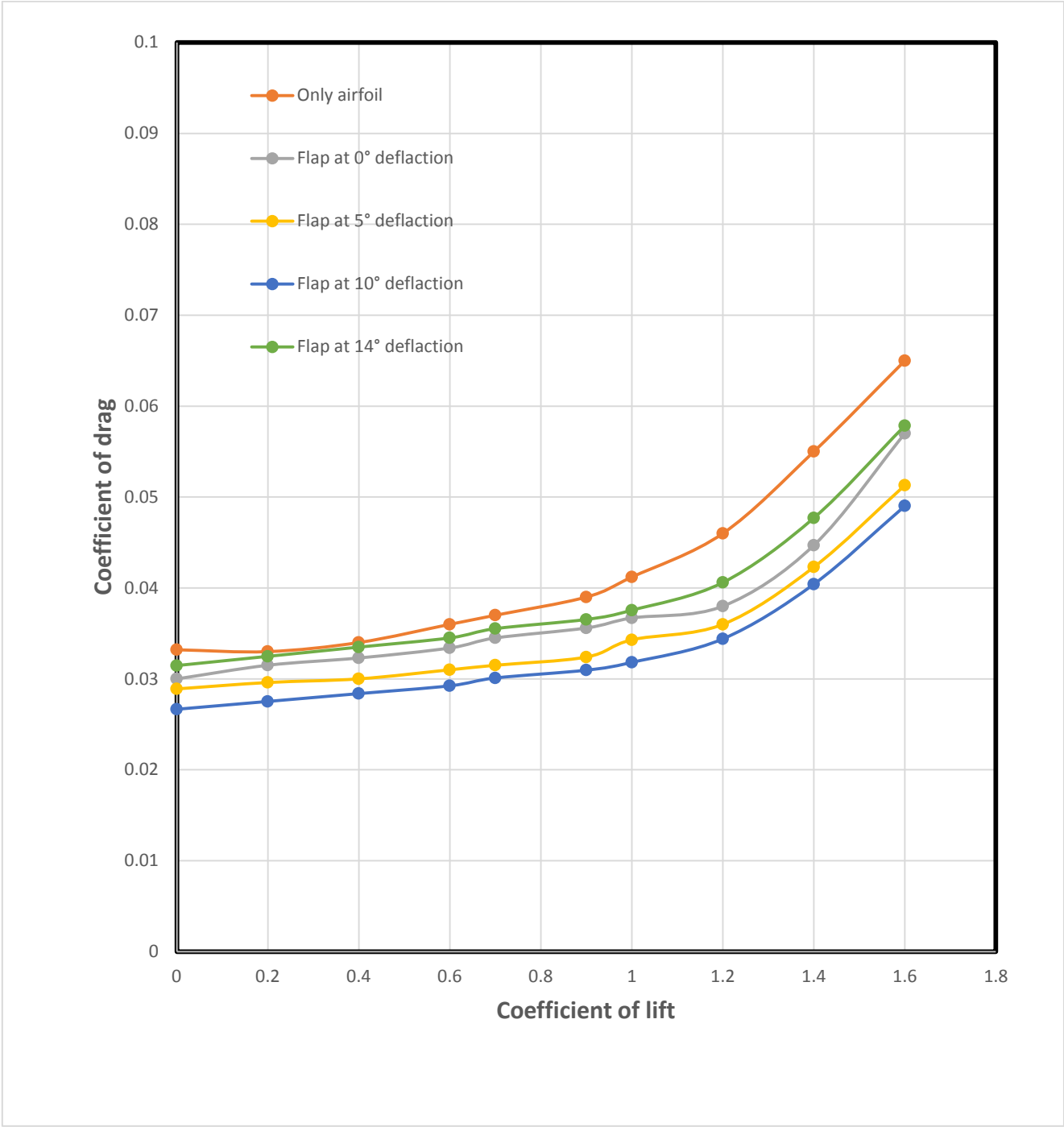

Figure-4.11: Comparison of coefficient of drag Vs coefficient of lift.

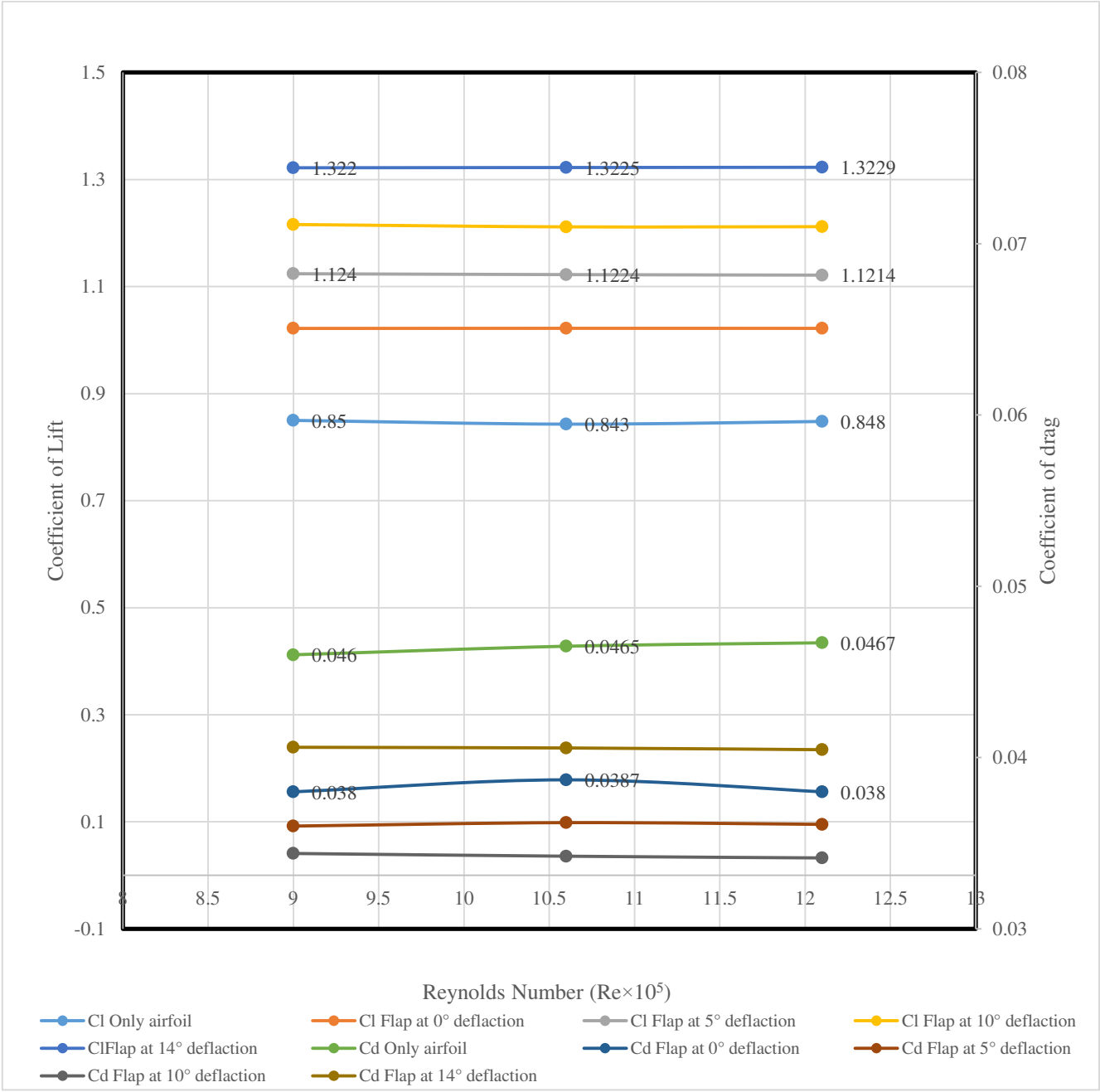

Figure-4.12: Effects on Reynolds Number with Coefficient of Lift and Coefficient of Drag

4.3 Discussion

The lift and drag coefficients as a function of the AOA for the baseline NACA0012 airfoil model were measured at Re_c=4.74x10^5. According to McCormick's formula [18], the lift slope depends on the aspect ratio (AR) by

$$a=\frac{dC_L}{d_\alpha}=\frac{a_o AR}{AR+2(AR+4)/(AR+2)} \quad \text{----------(4.3)}$$

where a_o =2π, according to thin-airfoil theory. A fit to the lift data of the baseline model using equation (4.3) gives the effective aspect ratio AR=4.42 that is larger than the physical aspect ratio of 1.2. The end plates substantially reduced the three-dimensionality of flow. The drag coefficient is represented as a function of the lift coefficient squared and fitted using the classical relation $C_D= C_{D0}+C^2_L/\pi eAR$. Therefore, we obtain the zero-lift drag coefficient C_{D0}=0.014 and the Oswald span efficiency e=0.8 for the baseline model with AR=4.42. Although the finite end plates do not completely eliminate the three-dimensionality of flow, they modify the tip vortices, acting like large winglets.

In tests, an aluminum sheet (0.216 mm thick) and a Mylar sheet (0.254 mm thick) were used as the SETE, for which the deflection angle was set a priori. The plate flexural rigidities of the aluminum sheet and Mylar sheet are D_E=0.067 and 0.0044Nm, respectively. Figure (4.9) and (4.10) shows the lift coefficient as a function of the AOA and drag polar for the model with the SETE at Re_c=4.74x10^5, where C_L and C_D are based on the projected wing area of the baseline model. The lengths of the SETE are 5 and 10% of the chord of the baseline model, and the preset deflection angles of the SETE are 0,5, and 10 degree. According to figure (4.9) and (4.11) the C_L distribution is shifted up and the lift is enhanced depending on the deflection angle and relative length of the SETE, whereas the drag polar basically remains unchanged. The drag polar curves are collapsed for different deflection angles, indicating that the zero-lift drag and Oswald's efficiency are not change much. Stall occurs a few degrees earlier, particularly for larger deflections. For the model with zero deflection, C_L is almost the same as that of the baseline model when the AOA is less than 10 degree, but it is larger for higher AOA until stall. Typically, four and five repeated tests were conducted for each case, and the results were averaged. The measurement uncertainties in C_L are 0.001 for low AOA and 0.01 for high AOA. For C_D, the measurement errors are 0.0002 for low AOA and 0.003 for high AOA. In general, the lift and drag coefficients for the SETE are normalized based on the main

airfoil chord rather than on the total projected chord that is a variable. For a direct comparison with other trailing-edge devices, both the main airfoil chord and total projected chord are used for normalization. It must be emphasized that the lift enhancement is mainly a result of an increase in the pressure difference across the main airfoil induced by the SETE due to the camber effect, and additional aerodynamic loading on the SETE itself is not significant.

Further, the drag coefficient is plotted as a function of the lift coefficient squared. All the data are basically collapsed into a single straight line, which is consistent with figure. Both the zero-lift drag coefficient and Oswald's efficiency do not significantly change within the measurement accuracy for different deflection angles and lengths of the SETE. It is indicated that the increased C_D results mainly from an increase of the induced drag $C^2_L/\pi eAR$ associated with the lift enhancement by the SETE. It is expected that this drag penalty will be reduced as the aspect ratio increases.

4.3.1 Comparison with Gurney Flaps

The aerodynamic characteristics of the SETE are compared with those of a Gurney flap, which is a short wall attached to the trailing edge that is perpendicular to the chord line on the pressure side of an airfoil. Both the SETE and Gurney flap increase the lift at the cost of increasing the drag. However, these are some important quantitative differences between the SETE and Gurney flaps on the drag penalty. The measured result by Li et al.[2] for a NACA0012 rectangular wing indicate that L/D as a function of C_L for the wing with Gurney flaps (0.5-3%-c heights) is significantly lower than that for the baseline wing except at higher C_L. Unlike the SETE, the curves of L/D as a function of C_L for Gurney flaps do not collapse. Similar results can be found for other wings with Gurney flaps. The general conclusion is that Gurney flaps are not suitable for cruise flight due to the reduced L/D by the larger drag penalty. After fitting the data of Li et al.[2] using $C_D= C_{D0}+C^2_L/\pi eAR$, it is found that the zero-lift drag coefficient C_{D0} increases in a roughly linear fashion from 0.0065 for the baseline model to 0.021 for the 3%-c high Gurney flap, for which the effective aspect ratio is 46.5. The drag increase is caused by the extra form drag associated with open flow separation behind a Gurney flap.

To provide a direct comparison of the SETE with Gurney flaps, Gurney flap measurements were conducted using the same baseline NACA0012 airfoil model with the same chord Reynolds number. The Gurney flap height ranges from 1.2 to 6.75% c. figure 4.12 shows the lift coefficient as a function of the AOA and drag polar for the model with Gurney flaps at $Re_c=4.74x10^5$. The C_L curve is shifted up depending on the Gurney flap height, but C_D increases considerably except for the cases with 1.2 and 2.0% c. The drag coefficient is plotted as a function of the lift coefficient squared. The plots for the heights 1.2 and 2% c are close to that for the baseline model, whereas other curves are considerably shifted and the slope is also changed. This indicates that the zero-lift drag coefficient increases and Oswald's efficiency varies for Gurney flaps. These results are similar to the previously published data for a NACA0012 airfoil [2]. The vertical displacement of the tip of the SETE is about 0.87% c, which is close to the Gurney flap height of 1.2% c. The lift enhancements in both cases are almost the same, but the Gurney flap suffers from a larger drag penalty, giving a smaller L/D than that for the SETE for all positive C_L.

To evaluate the net benefit of flow control in terms of the power required for cruise flight, Liu [2] proposed the following weight criterion:

$$\left[1+\frac{6}{7}\left(\frac{\eta_{FC,r}}{b}\frac{C_L^{\frac{3}{2}}}{C_D}\right)W^{-\frac{1}{6}}\right]^{-1}\left(-\frac{6}{7}\frac{\Delta C_D}{C_D}+\frac{9}{7}\frac{\Delta C_L}{C_L}\right)-\frac{\Delta W}{W}>0 \text{----------(4.4)}$$

Where $\Delta W/W$ is the ratio between the control system weight ΔW and the total aircraft weight W, and $\eta_{FC,r}=P_{FC,r}/\Delta W$ is the actuating power density. For an ideal weightless passive control device, the criterion is reduced to

$$-\frac{6}{7}\frac{\Delta C_D}{C_D}+\frac{9}{7}\frac{\Delta C_L}{C_L}=g>0 \text{----------(4.5)}$$

The function g is interpreted as a benefit margin for flow control. When g is positive, less engine power is required for cruise flight with passive flow control devices such as the SETE and Gurney flaps, and therefore the net benefit is achieved. For the SETE of the 10%-c length and deflection angle of 5 degree, its benefit margin remains positive and approaches zero as the AOA reaches 13 degree. This further confirms the feasibility of this SETE for improving the cruise flight efficiency. In contrast, for the 10%-c SETE with a deflection of 14 degree, the benefit margin becomes negative at about a 5 degree AOA. The Gurney flap with the 1.2%-c

height has a similar behavior, whereas for the Gurney flap with the 4.12%-c height, g is considerably below zero after about a 3 degree AOA.

4.3.2 Thin-Airfoil Theory

Like conventional flaps, the lift enhancement by the SETE is generated by a change of the camber at the trailing edge. For geometrical simplicity, the main wing and SETE are modeled by straight segments. The total projected chord is $c'=c+l\cos\delta$. The slopes of the chord line segments are 0 for $0\leq x<c$ and $-\tan\delta$ for $c\leq x<c'$. According to the classical thin-airfoil theory assuming that the slope is small, the strength of the vortex sheet is

$$\gamma(\theta)=2U_\infty\left(A_0\frac{1+\cos\theta}{\sin\theta}+\sum_{n=1}^{\infty}A_n\sin n\theta\right)\text{----------(4.6)}$$

Where the angular variable is related the main chord wise coordinate by $x=(c'/2)(1-\cos\theta)$. The coefficients in equation 4.6 are $A_0=\alpha+\tan\delta(1-\theta_c/\pi)$ and $A_n=(2/\pi n)\tan\delta\sin(n\theta_c)$ $(n=1,2,\ldots.)$. Here, the angular variable θ_c, which corresponds to the breaking point between the main wing and SETE, is given by $\theta_c=\cos^{-1}[(\varepsilon-1)/(\varepsilon+1)]$, where $\varepsilon=(1/c)\cos\delta$.

The sectional lift coefficient is given by

$$C_l=\frac{L'}{(1/2)\rho_\infty U_\infty^2 c}=2\pi(1+\varepsilon)[\alpha+\tan\delta(1-\theta_c/\pi+\sin\theta_c/\pi)]\text{----------(4.7)}$$

The positive deflection angle of the SETE shifts the C_l curve upward (lift enhancement) and slightly increases the lift slope. The moment coefficient around the one-fourth total chord is

$$C_{m,c'/4}=\frac{M'_{c'/4}}{\left(\frac{1}{2}\right)\rho_\infty U_\infty^2 c^2}=(1/4)(1+\varepsilon)^2\tan\delta(\sin2\theta_c-2\sin\theta_c)\text{----------(4.8)}$$

Where $C_{m,c'/4}$ is defined to be positive when it is the nose-up moment. Clearly, the positive deflection angle produces a negative moment. Furthermore, the pressure coefficient difference between the pressure and upper surfaces of the airfoil is $\Delta C_p=2\gamma(x)/U_\infty$. For a finite rectangular wing, the effective angle of attack is $\alpha-(1+\tau)C_L/\pi AR$, where AR is the effective aspect ratio and the parameter τ is a function of $AR/2\pi$ for a rectangular wing. A convenient regression formula is $\tau=-0.0476(AR/2\pi)^2+0.2195(AR/2\pi)$ for $AR/2\pi\ \epsilon[0.25, 1.75]$. Hence, the lift enhancement $\Delta C_L=C_L-C_{L,baseline}$ for a finite rectangular wing can be calculated, where the lift coefficient for the wing with the SETE and baseline wing are, respectively,

$$C_L=\left[1+\frac{2(1+\tau)}{AR}\right]^{-1}C_l\text{----------(4.9)}$$

And

$$C_{L,baseline}=[1+\frac{2(1+\tau)}{AR}]^{-1}2\pi\alpha\text{----------(4.10)}$$

According to the preceding relations, the lift enhancement by the SETE is

$$\Delta C_L=2[1+\frac{2(1+\tau)}{AR}]^{-1}[\pi\varepsilon\alpha+(1+\varepsilon)\tan\delta(\pi-\theta_c+\sin\theta_c)]\text{----------(4.11)}$$

The difference of the pressure coefficient between the pressure and upper surfaces of the main wing is sensitively affected by the SETE. These results indicate a direct correlation of the aerodynamic loading between the main airfoil and the SETE. The near-linear relation given by thin-airfoil theory reasonably describes the initial trend of the experimental results for small deflections. However, the experimental data saturate as the deflection angle increases further, which may be caused by a reduced effective deflection due to the viscous effect. Two dimensional CFD calculations using a Navier-Stokes code (Fluent), assuming that the boundary layer on the NACA0012 airfoil with the SETE is fully turbulent, predict the smaller lift enhancement.

Thin airfoil theory has been expanded for the lift problem of an airfoil with a Gurney flap. A solution of the generalized thin airfoil integral equation for the vortex strength can be obtained by the method of successive approximations. The Gurney flap lift enhancement is interpreted as a special camber effect. The lift coefficient increment (pitching moment as well) is given as a square-root function of the relative Gurney flap height (i.e., $\Delta C_L \alpha \sqrt{h/c}$). For comparison with the Gurney flap, the vertical displacement of the SETE is defined as $h/c=(l/c)\sin\delta$. Therefore, ΔC_L by the SETE depends on the relative length l/c and deflection angle δ. Interestingly, ΔC_L increases in a linear fashion as an increase of the deflection angle for the SETE with a fixed length, whereas ΔC_L follows a square-root relation for both the Gurney flap and the SETE, with a variable length for a fixed deflection angle.

CHAPTER-5

Conclusions

Experiments and calculations presented show that a static extended trailing edge (SETE) attached to a NACA0012 airfoil model is able to enhance the lift, whereas the zero-lift drag is not significantly increase. The lift enhancement mechanism by the SETE is the camber effect, which is the same as that for other high-lift devices such as a Gurney flap and conventional flap. However, compared with a Gurney flap and conventional flap, the SETE generates a larger lift increase at a smaller drag penalty because it is embedded in the wake of the main airfoil. Therefore, the SETE has a promising potential for improving the cruise flight efficiency. The benefit margin of the SETE for cruise flight is evaluated in comparison with the Gurney flap, and the feasibility of the SETE for lift enhancement in cruise flight is demonstrated at small angles of attack and deflection angles of the SETE. The mechanical simplicity of the SETE allows direct application to aircraft without changing the basic aerodynamic configuration. Furthermore, the deformation and pitching moment of the SETE due to aerodynamic loading are estimated, and actuating the SETE is feasible because the pitching moment on it is small. Future research will focus on the SETE actuation using smart materials such as piezoactuators and shape memory alloys for steady and unsteady flow control. The overall achievement of this thesis is given below,

- There is no effect on Reynolds numbers
- Drag reduced approximately 20% when flap deflection at 10^0
- Lift enhanced almost 20% when flap deflection at 10^0
- Stall delayed 12^0 to 14^0

REFERENCES

[1] Liebeck, R. H., “Design of Subsonic Airfoils for High Lift,” Journal of Aircraft, Vol. 15, No. 9, 1978, pp. 547-561.

[2] Liu, T., Kuykendoll, K., Rhew, R. and Jones, S., “Avian Wing Geometry and Kinematics,” AIAA Journal, Vol. 44, No. 5, 2006, pp. 954-963.

[3] Garner, P.L., Meredith, P.T., and Stoner, R.C., “Areas for Future CFD Development as Illustrated by Transport Aircraft Applications,” AIAA Paper 91-1527, 1991.

[4] Van Dam, C.P.; Yen, D.T.; Vijgen, P. (1999). "Gurney flap experiments on airfoil and wings". Journal of Aircraft (0021-8669) 36 (2): 484–486. doi:10.2514/2.2461.

[5] Storms, B.L.; Jang, C.S. (1994). "Lift Enhancement of an Airfoil Using a Gurney Flap and Vortex Generators". Journal of Aircraft 31 (3): 542–547. doi:10.2514/3.46528.

[6] Tianshu Liu, J. Montefort, W. Liou, S. R. PantulaandQamar A. Shams; “Static Extended Trailing Edge for Lift Enhancement: Experimental and Computational Studies,” 3rdInternational Symposium on Integrating CFD and Experiments in Aerodynamics.

[7] Gai, S. L. and Palfrey, R., “Influence of Trailing-Edge Flow Control on Airfoil Performance,” Journal of Aircraft, Vol. 40, No. 2, 2003, pp. 332-337.

[8] McCormick, B. W., “Aerodynamics, Aeronautics, and Flight Mechanics (Second Edition),” John Wiley &Sons, New York, 1995, p. 116.

[9] Meyer, R., Hage, W., Bechert, D.W., Schatz, M. and Thiele, F., “Drag Reduction of Dimensional Modification,” Journal of Aircraft, Vol. 43, No. 1, 2006, pp. 132-140.

[10] Storms, B. and Ross, J., “Experimental Study of Lift-Enhancement Tabs on a Two-Element Airfoil,” Journal of Aircraft, Vol. 32, 1995, pp. 1072-1078.

[11] Lee, H. T., Kroo, I. M., and Bieniawski, S., “Flutter Suppression for High Aspect Ratio Flexible Wings Using Microflaps,” AIAA Paper 2002-1717, Denver, CO; 22-25 Apr. 2002.

[12] Stanewsky, E., “Adaptive Wing and Flow Control Technology,” Progress in Aerospace 37, 2001, pp. 583-667.

[13] D.P. Jansen,Passive Flow Separation Controlon an Airfoil-Flap ModelThe Effect of Cylinders and Vortex Generators. Delft University of Technology, August 2012.

[14] J. C. Lin. Control of turbulent boundary-layer separation using micro-vortex generators. AIAA Journal, 3404:99, 1999.

[15] J. Little, M. Nishihara, I. Adamovich, and M. Samimiy. Separation control from the flap of a high-liftairfoil using DBD plasma actuators. In AIAA Paper 2009-145, 2009.

[16] V. Maldonado, J. Farnsworth, W. Gressick, and M. Amitay. Active control of flow separation and structural vibrations of wind turbine blades. *Wind Energy*, 13:221–237, 2010.

[17] P.T. Meredith. Viscous phenomena affecting high-lift systems and suggestions for future CFD develop-ment. In AGARD CP-515, 1992.

[18] L.M.M. Boermans and P.B. Rutten. Two-dimensional aerodynamic characteristics of airfoil NLF-MOD22with fowler flap. Technical report, TU Delft, 1995

[19] M.V. van der Steen. Passive off-surface flow separation control methods on a simplified flapped configuration. Master's thesis, TU Delft, 2009